

Internal Waves in Monterey Submarine Canyon

ERIC KUNZE

Applied Physics Laboratory, University of Washington, Seattle, Washington

LESLIE K. ROSENFELD

Naval Postgraduate School, Monterey, California

GLENN S. CARTER AND MICHAEL C. GREGG

Applied Physics Laboratory, University of Washington, Seattle, Washington

(Manuscript received 6 June 2001, in final form 15 November 2001)

ABSTRACT

Velocity, temperature, and salinity profile surveying in Monterey Submarine Canyon during spring tide reveals an internal wave field almost an order of magnitude more energetic than that in the open ocean. Semidiurnal fluctuations and their harmonics dominate, near-inertial motions are absent. The ratio of horizontal kinetic to available potential energy is less than one in much of the canyon, inconsistent with hydrostatic internal waves. The excess potential energy may be due to isopycnal displacements induced by barotropic tide flow over the sloping bottom. Removal of the expected barotropic contribution raises the energy ratio to 2.04–2.10, in line with the semidiurnal internal wave value of 2.13. Finescale shear and strain are also elevated. Finescale parameterizations for turbulent eddy diffusivities, which have proven successful in the open ocean, underestimate upper-canyon microstructure estimates of $100 \times 10^{-4} \text{ m}^2 \text{ s}^{-1}$ by a factor of 30. Energy fluxes and near-bottom velocities are strongly steered by the sinuous canyon topography. A vertically integrated influx of 5 kW m^{-1} at the mouth diminishes to $\pm 1 \text{ kW m}^{-1}$ toward the shallow end of the canyon. Both sinks and sources of internal wave energy are indicated by energy-flux convergences and divergences along the canyon axis. Along-axis energy-flux convergences are consistent with microstructure dissipation rates ϵ . The high diapycnal eddy diffusivities may drive strong nutrient fluxes to enhance bioproductivity.

1. Introduction

Submarine canyons are common features of continental margins with dozens found off both coasts of the continental United States (Shephard et al. 1979; Hunkins 1988). They incise 20% or more of the Pacific North American shelf between the equator and Alaska, approaching 50% at latitudes north of 45° (Hickey 1995). They are often avoided by coastal observational programs because their short horizontal scales make them difficult to characterize with a few point measurements.

Far from being backwaters, canyons contain large physical, geological, and biological signals. They have been cited as sediment pathways off the shelf (Shephard et al. 1974; Carson et al. 1986) and argued to be sites of enhanced species diversity and bioproductivity based largely on anecdotal evidence of intense

fishing activity and marine mammal/bird aggregations. This last is far from certain, however. While Schoenherr (1991) and Croll et al. (2001, manuscript submitted to *Ecology*) report blue whales feeding on high concentrations of euphausiids in Monterey Submarine Canyon, a survey of the northeast U.S. continental shelf finds no evidence for greater cetacean densities in canyons (Kenney and Winn 1987). Croll et al. attribute high euphausiid concentrations to the juxtaposition of upwelling upstream to the north (Rosenfeld et al. 1994a) and a deep water column allowing full diel vertical migration. Euphausiids may also be concentrated by horizontal convergences (Allen et al. 2001).

It has been suggested that bioproductivity in canyons could be enhanced by upwelling (Freeland and Denman 1982) because upwelling-favorable shelf currents produce unbalanced upcanyon pressure gradients $\partial p/\partial x$ in narrow canyons that drive upcanyon flow $\partial u/\partial t$. Theoretical and numerical studies (Klinck 1988, 1989, 1996; Allen 1996; Chen and Allen 1996) have shown that strong upwelling occurs on the downstream rim of can-

Corresponding author address: Dr. Eric Kunze, Applied Physics Laboratory, University of Washington, 1013 NE 40th St., Seattle, WA 98105-6698.
E-mail: kunze@ocean.washington.edu

yons narrower than half the Rossby radius; in broader canyons, geostrophic flow is predicted to follow isobaths as observed (Kinsella et al. 1987; Maso et al. 1990).

An alternative but unexplored mechanism for supplying nutrients to the euphotic zone is enhanced turbulent mixing. In the stratified ocean, turbulence is largely controlled by the rate at which energy is transferred through the internal wave spectrum to high vertical wavenumbers. Enhanced turbulence requires either an elevated internal wave field or elevated spectral transfer rates.

Canyons may be both effective conduits for funneling open-ocean internal wave energy onto the inner shelf (Gordon and Marshall 1976) and sites for generation of internal waves through topographic scattering of surface tides (Bell 1975; Baines 1982, 1983). Due to the reflection behavior of internal waves off sloping bottoms, canyon geometry should deflect low-frequency waves toward the deep ocean while trapping and focusing internal waves with frequencies $\omega > [(f^2 + N^2\alpha^2)/(1 + \alpha^2)]^{1/2}$ toward the heads of canyons (Wunsch 1968, 1969; Cacchione and Wunsch 1974; Hotchkiss and Wunsch 1982), where f is the Coriolis frequency, N the buoyancy frequency, and α the canyon axis bottom slope. Trapping should produce a highly anisotropic wave field. Waves with frequencies near $\omega_c = [(f^2 + N^2\alpha^2)/(1 + \alpha^2)]^{1/2}$ will be critically reflected toward high wavenumber (Eriksen 1982). Critical reflection amplifies internal wave energy, shear, and strain near the bottom. In Monterey Canyon, the axis slope is ~ 0.06 in the deep part of the canyon, close to critical for the semidiurnal frequency, becoming supercritical (steeper) at axis depths shallower than ~ 400 m. The canyon walls are much steeper. Bottom roughness will scatter internal waves toward high wavenumber (Müller and Xu 1992; Thorpe 2001).

Internal wave fluctuations dramatically larger than those in the open ocean have been reported in canyons (Shepherd et al. 1974; Gardner 1989; Hotchkiss and Wunsch 1982; Petrucio et al. 1998; Garcia Lafuente et al. 1999). Hotchkiss and Wunsch (1982) reported available potential energy increasing by a factor of 10 toward the bottom and 100 toward the head of Hudson Canyon. Near-inertial oscillations are suppressed by the proximity of steep topography, while internal tides and their harmonics are enhanced to velocities in excess of 30 cm s^{-1} . In Monterey Submarine Canyon, semidiurnal oscillations in excess of 20 cm s^{-1} dominate (Rosenfeld et al. 1994b; Kinoshita and Noble 1995), amplified toward the bottom and head of the canyon (Xu et al. 2002). Shepherd et al. (1979) reported similar values from current-meter measurements in 63 separate canyons. Butman (1986) found that the dominant semidiurnal oscillations in Lydonia Canyon diminished toward the head in concert with amplifying higher-frequency fluctuations.

The prominent semidiurnal peak in canyons is con-

sistent with near-critical reflection (Eriksen 1982) or topographic scattering of the surface tide (Baines 1982; Craig 1987). Petrucio et al. (1998) describe a bottom-hugging semidiurnal beam propagating up Monterey Canyon during one sampling interval but standing in the along-axis direction during another. They reported that 90% of the velocity ($\pm 20 \text{ cm s}^{-1}$) and isopycnal displacement ($\pm 20 \text{ m}$) variance in the water column could be explained by semidiurnal oscillations. Because the axis slope is comparable to the semidiurnal characteristic slope, an amplified internal tidal beam hugging the axis bottom is expected rather than a vertically standing mode since modal vertical structure could only set up after the beam contacts the surface, in water depths less than 400 m. This is consistent with high-frequency radar measurements (Paduan and Rosenfeld 1996; Petrucio et al. 1998), which show the strongest semidiurnal surface currents inshore of the 200-m isobath.

Enhanced internal wave energy in canyons should drive elevated turbulence and mixing. Itsweire et al. (1989) described 10–15-m-thick layers of high shear and turbulent dissipation rate in upper thermocline waters of Monterey Canyon but these were not dissimilar to features found in the open ocean. Lueck and Osborn (1985) observed up to 170-m thick stratified turbulent bottom boundary layers on the south wall of Monterey Canyon with eddy diffusivities of up to $15 \times 10^{-4} \text{ m}^2 \text{ s}^{-1}$, two orders of magnitude higher than open-ocean values. These turbulence levels are consistent with Hotchkiss and Wunsch's (1982) predictions in Hudson Canyon based on their inferred upcanyon energy flux. Based on measured upcanyon energy-flux divergence, Petrucio et al. inferred turbulence production rates of $(0.13\text{--}2.3) \times 10^{-6} \text{ W kg}^{-1}$, corresponding to eddy diffusivities of $O(100 \times 10^{-4} \text{ m}^2 \text{ s}^{-1})$. Similar values have been reported above seamounts (Nabatov and Ozmidov 1988; Lueck and Mudge 1997; Kunze and Toole 1997).

In this paper, internal wave energetics in Monterey Submarine Canyon are investigated using repeated velocity, temperature, and salinity profile surveys. Monterey Canyon's channel meanders from within a stone's throw of the dock at Moss Landing, across the Monterey Bay shelf and down the continental slope, extending hundreds of kilometers offshore. Its width (as defined by the 150-m isobath) varies from about 15 km at the shelf break to 2 km at its head. On the shelf, its axis slope is near-critical for the semidiurnal frequency while its walls are considerably steeper. The surface tide cooscillates across Monterey Bay with barotropic velocities in the canyon less than 1 cm s^{-1} (Petrucio et al. 1998). Surface currents of $\pm 15 \text{ cm s}^{-1}$ are dominated by semidiurnal internal oscillations 180° out of phase with the barotropic currents and oriented parallel to isobaths (Paduan and Rosenfeld 1996).

Sampling and data processing to obtain vertical displacements ξ and energy fluxes $\langle \nu'p' \rangle$ are described in section 2. Section 3 presents frequency spectra from the deeper acoustic Doppler current profiler (ADCP) moor-

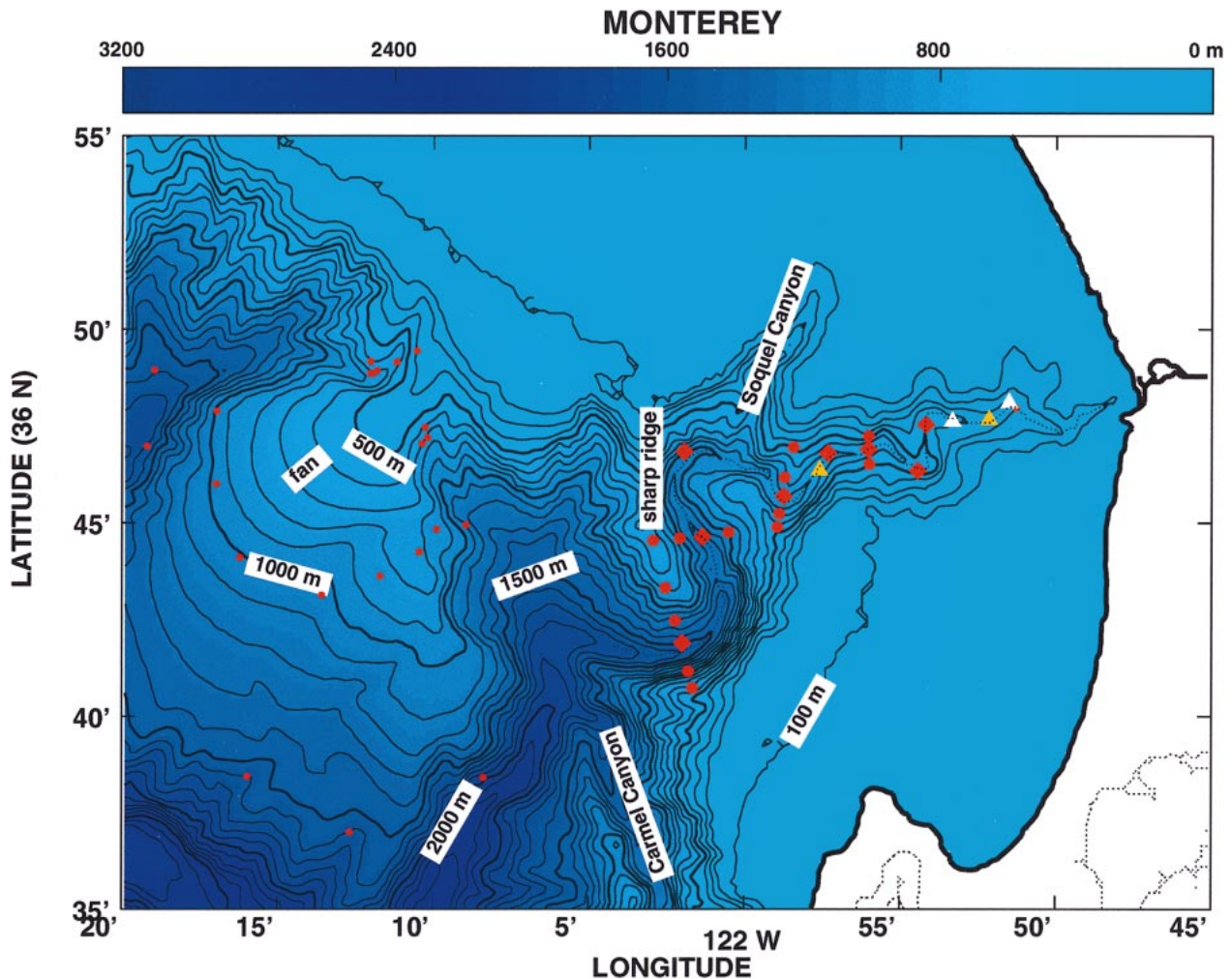


FIG. 1. Sampling in Monterey Submarine Canyon. Large red diamonds correspond to XCP-XCTD stations along the canyon axis occupied eight times during two 12-h periods separated by a day, large red dots to four across-canyon sections occupied four times during 12 h, and small red dots on the continental slope to the north of the canyon mouth to single XCP-XCTD pairs. Upward-looking ADCP moorings (white triangles) and CTD time series (orange triangles) were located at the shallow end of the canyon. The deeper ADCP was moored slightly off axis.

ing; mooring data and numerical simulations are described in greater detail in Rosenfeld and Kunze (1998), Rosenfeld et al. (1999), and Key (1999), emphasizing an internal tidal bore propagating upcanyon along the axis and hysteresis effects in the near-bottom tidal flow due to topographic steering. In section 4, along- and acrosscanyon sections of larger-scale energy, and fine-scale shear and strain, are presented. Finescale turbulence parameterizations are found to fall short of direct microstructure estimates by a factor of 30 in section 5. Section 6 describes energy fluxes and section 7 an energy budget comparing energy-flux convergences and divergences along the canyon axis with microstructure turbulent dissipation rates. Results are summarized in section 8 followed by discussion in section 9.

Additional fine- and microstructure data collected at the shallow end of the canyon are reported by Carter

and Gregg (2001, manuscript submitted to *J. Phys. Oceanogr.*, hereafter CG) and over a submarine fan north of the canyon mouth by Lien and Gregg (2001). Carter and Gregg report that available potential energy PE decreases toward the head, horizontal kinetic energy KE decreases then increases, and that turbulent dissipation rates ϵ and eddy diffusivities K do not increase toward the head. Globally, they suggest that 58 GW might be dissipated in canyons. Lien and Gregg report evidence of a tidal beam emanating from the shelf break to the north of the canyon with elevated turbulent dissipation rates $\epsilon \sim 10^{-5} \text{ W kg}^{-1}$ and eddy diffusivities $K \sim (10\text{--}1000) \times 10^{-4} \text{ m}^2 \text{ s}^{-1}$, and a 100-m thick near-bottom layer of intensified turbulence ($\epsilon \sim 10^{-6} \text{ W kg}^{-1}$, $K \sim 100 \times 10^{-4} \text{ m}^2 \text{ s}^{-1}$) driven by hydraulic semidiurnal flow across the submarine fan. They suggest 31 GW of dissipation for the shelf break globally. Dis-

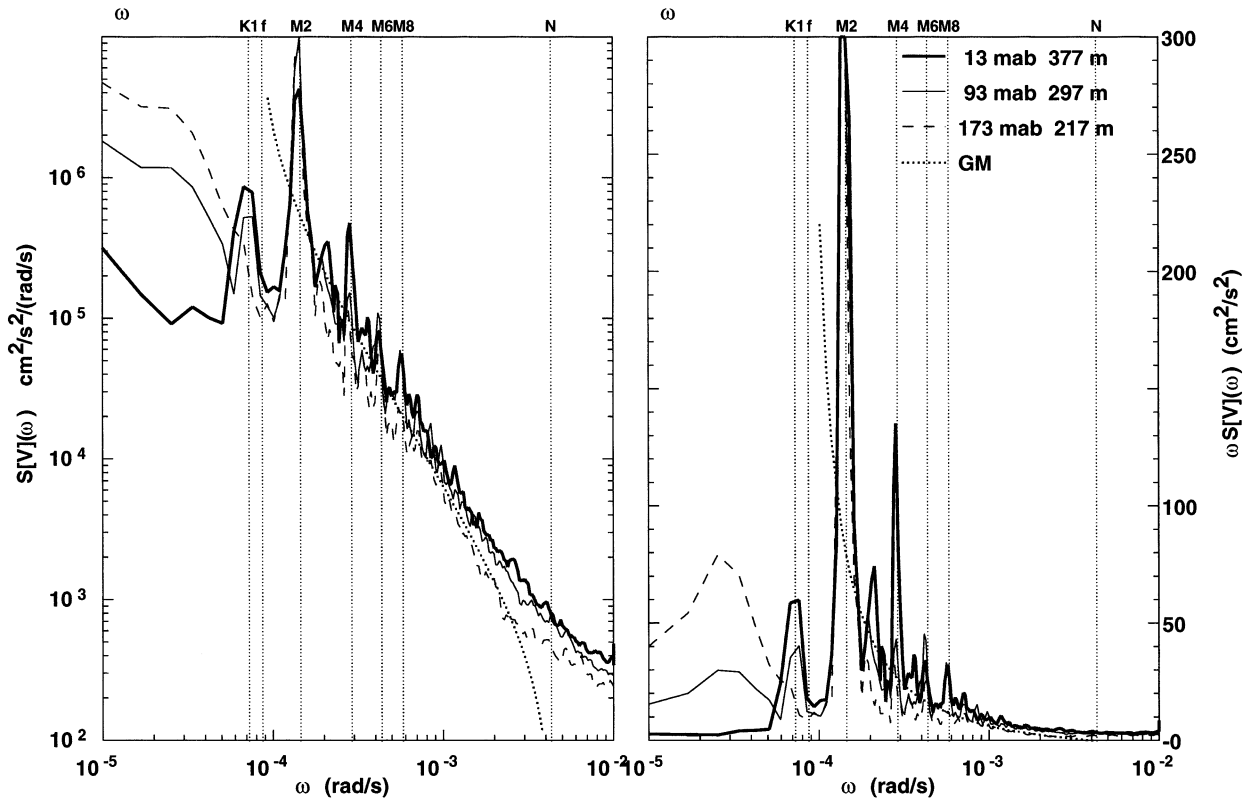


FIG. 2. Frequency spectra for velocity from the deeper ADCP mooring (Fig. 1) in (left) log-log and (right) variance-preserving formats; the lowest resolved frequency 1.8×10^{-4} rad s^{-1} is not plotted. Records come from bins 13–173 mab (meters above bottom). Observed spectra are comparable to the Garrett and Munk (GM; 1979) model (dotted curves) except (i) at the inertial frequency f where a peak is absent, (ii) at the semidiurnal frequency M_2 where there is a strong peak at all depths, (iii) at harmonics of the semidiurnal and diurnal frequencies where there are smaller peaks that diminish with height above bottom, and (iv) near the buoyancy frequency N where there is excess energy diminishing with height above bottom. There is no sharp break in the spectra near the buoyancy frequency. There is also energy at the diurnal frequency K_1 , which decays away from the bottom, and at periods of 3–4 days, which increases with height above bottom.

sipation rates $\epsilon \sim 5 \times 10^{-8}$ W kg^{-1} and eddy diffusivities $K < 10^{-4}$ m 2 s^{-1} are found on the shelf.

2. Data

a. Sampling

During a two-week period of exceptionally light winds (CG01) in August 1997, the internal wave and turbulence fields in Monterey Submarine Canyon were sampled with a suite of fine- and microstructure instruments. Full-depth profiles of velocity, temperature, and salinity were collected during the spring tide at 21 stations along and across the canyon with 101 expendable current profiler–expendable CTD (XCP–XCTD) pairs (large red dots and diamonds, Fig. 1) spanning canyon axis depths of 300–1600 m. The deepest across-canyon section was at the shelf break, which will be referred to as the “canyon mouth.” Cross-canyon stations (large red dots) were occupied four times in 12 h to obtain statistics of the internal wave field. Stations along the canyon axis (large red diamonds) were occupied eight times during two 12-h periods separated by a day. In

addition, 33 single XCP–XCTD pairs were deployed along the 1000- and 1500-m isobaths on the submarine fan and continental slope to the north of the canyon mouth (small red dots).

Two upward-looking ADCPs were deployed at the shallow end of the canyon (white triangles, Fig. 1) for 36 days bracketing the cruise (Key 1999). Four 12-h long CTD time series (orange triangles, Fig. 1) were conducted, two near the 400-m isobath between the ADCP moorings, and two near axis depths of 800 m. Finally, 66 expendable dissipation probes (XDPs) were deployed but these provided no usable data.

The Sippican expendable current profiler measures horizontal velocity relative to an unknown but depth-independent constant by measuring the voltage drop across the probe’s insulating body induced by the electric field due to the movement of conducting seawater in the earth’s magnetic field (Sanford et al. 1982, 1993). Temperature is measured with an XBT thermistor. The XCP measures from the surface to ~ 1600 m depth. In the canyon measurements, all profiles measured to the bottom. Depth is calculated from a time-dependent fall

speed formula. At a fall speed of $\sim 5 \text{ m s}^{-1}$, velocity and temperature are sampled every 0.3 m. Typical rms uncertainties in 2-m binned velocity estimates are 0.5 cm s^{-1} . This cruise was the first scientific deployment of Sippican's new surface float design. Roughly a third of the probes failed to drop in the early part of the cruise until we consulted Sippican and made modifications to the probe release mechanism. Subsequently, this failure mode accounted for very little loss of data.

The Sippican expendable CTD measures temperature and conductivity from the surface to $\sim 1000 \text{ m}$ depth. Quoted uncertainties are $\pm 0.03^\circ\text{C}$, $\pm 0.03 \text{ msiemens cm}^{-1}$, and $\pm 2\%$ for temperature, conductivity, and depth, respectively.

b. Isopycnal displacements ξ

Vertical displacement profiles $\xi(z)$ were constructed from XCTD density and XCP temperature profiles relative to averages over the canyon survey, $\langle z(\sigma_\theta) \rangle$ and $\langle z(\theta) \rangle$, where 1000 points between minimum and maximum observed values were used for the σ_θ and θ coordinate grids and $\langle \cdot \rangle$ denotes a survey-wide or station average. The displacement versus density (temperature) profiles were then assigned to the mean depth $\langle z \rangle$ and interpolated onto the same 2-m depth grid as the processed XCP profiles. Simultaneous isotherm and isopycnal displacement profiles from the XCP and XCTD agree closely for most profile pairs. Isotherm and isopycnal displacements had rms values of 15–30 m while differing by less than 4–10 m. Differences could usually be attributed to water mass variability. Near-surface and -bottom points were included in this analysis since permanent well-mixed boundary layers were at most a few meters thick—that is, the entire water column was continuously stratified and able to support internal gravity waves; thicker layers of weak stratification were not evident in more than one profile of a time series, reminiscent of layering found above Fieberling Guyot, which was shown to be due to internal wave straining rather than turbulent mixing (Kunze and Toole 1997). Station-average profiles differed little from survey averages. For axis depths shallower than 550 m, CG reported similar continuous stratification during the spring tide, but weaker and more variable layered stratification during neap. Turbulent mixing could not account for the change in stratification, which they argued was largely due to advection.

In the analysis that follows, XCTD isopycnal displacements ξ are used above 900-m depth, XCP isotherm displacements below 1000-m depth, and a smoothly varying linear combination of the two in the 900–1000-m depth interval. While historical CTD profiles from the area (Rosenfeld et al. 1994c) show a tight T , S relation, vertical displacements below 1000-m depth may be overestimated because of water mass variability as well as instrument noise coupled with weak mean gradients.

c. Energy fluxes $\langle \tilde{u}\tilde{p} \rangle_\phi$

For internal gravity waves, the energy flux $C_g E = \langle \tilde{u}\tilde{p} \rangle_\phi$, where $C_g = \partial\omega/\partial k$ is the group velocity, E the wave energy, \tilde{u} indicates the wave velocity vector, $\tilde{p} = \tilde{P}/\rho_0$ the wave-induced reduced pressure anomaly, \sim the internal wave component, and $\langle \cdot \rangle_\phi$ denotes an average over wave phase. Baroclinic horizontal energy-flux profiles were constructed by combining vertically demeaned (baroclinic) horizontal velocity profiles $[\tilde{u}(z), \tilde{v}(z)]$ with vertically demeaned (baroclinic) reduced pressure anomaly profiles $\tilde{p}(z)$. Semidiurnal vertical velocity profiles $\tilde{w}(z)$ were estimated from semidiurnal fits to the vertical displacement profiles, $\tilde{w} = -i\omega\xi$. The pressure anomalies were computed from the survey-average stratification $\overline{N}^2(z)$ and the vertical displacement profiles $\xi(z)$ assuming a hydrostatic balance

$$0 = -\frac{\partial\tilde{p}}{\partial z} + \tilde{b}$$

and integrating with depth,

$$\begin{aligned} \tilde{p}(z) &= -\int_z^0 \tilde{b}(z') dz' + \tilde{p}(0) \\ &= -\int_z^0 \tilde{b}(z') dz' + \frac{1}{H} \int_{-H}^0 \int_z^0 \tilde{b}(z') dz' dz \\ &= \int_z^0 \overline{N}^2(z')\xi(z') dz' - \frac{1}{H} \int_{-H}^0 \int_z^0 \overline{N}^2(z')\xi(z') dz' dz, \end{aligned} \quad (1)$$

where buoyancy $\tilde{b} = -\overline{N}^2\xi$. The depth average (second term on rhs) is subtracted to satisfy the baroclinic condition for free internal waves of zero depth-average pressure anomaly; this condition may not hold in regions of direct forcing. The hydrostatic balance is valid for frequencies $\omega \ll N$, so should hold for the dominant semidiurnal fluctuations but might not be valid for the higher harmonics found near the bottom. A similar approach was used by Holloway (1996), Cummins and Oey (1997), and Garcia Lafuente et al. (1999), but their calculations do not satisfy the baroclinic condition on pressure. This does not affect estimates of depth-integrated baroclinic energy fluxes but impacts the vertical distribution, producing fluxes of the wrong sign in the upper water column and of the right sign but too strong in the lower water column for a dominantly mode-one energy flux.

3. Time series

Frequency spectra for velocity at three depths from the ($390 \pm 5 \text{ m}$ isobath) narrowband ADCP mooring (deeper white triangle, Fig. 1) are shown in (Fig. 2). This mooring was located slightly off-axis. Half-overlapping 4-day segments of the 36-day records were Fourier transformed and averaged together. In the internal

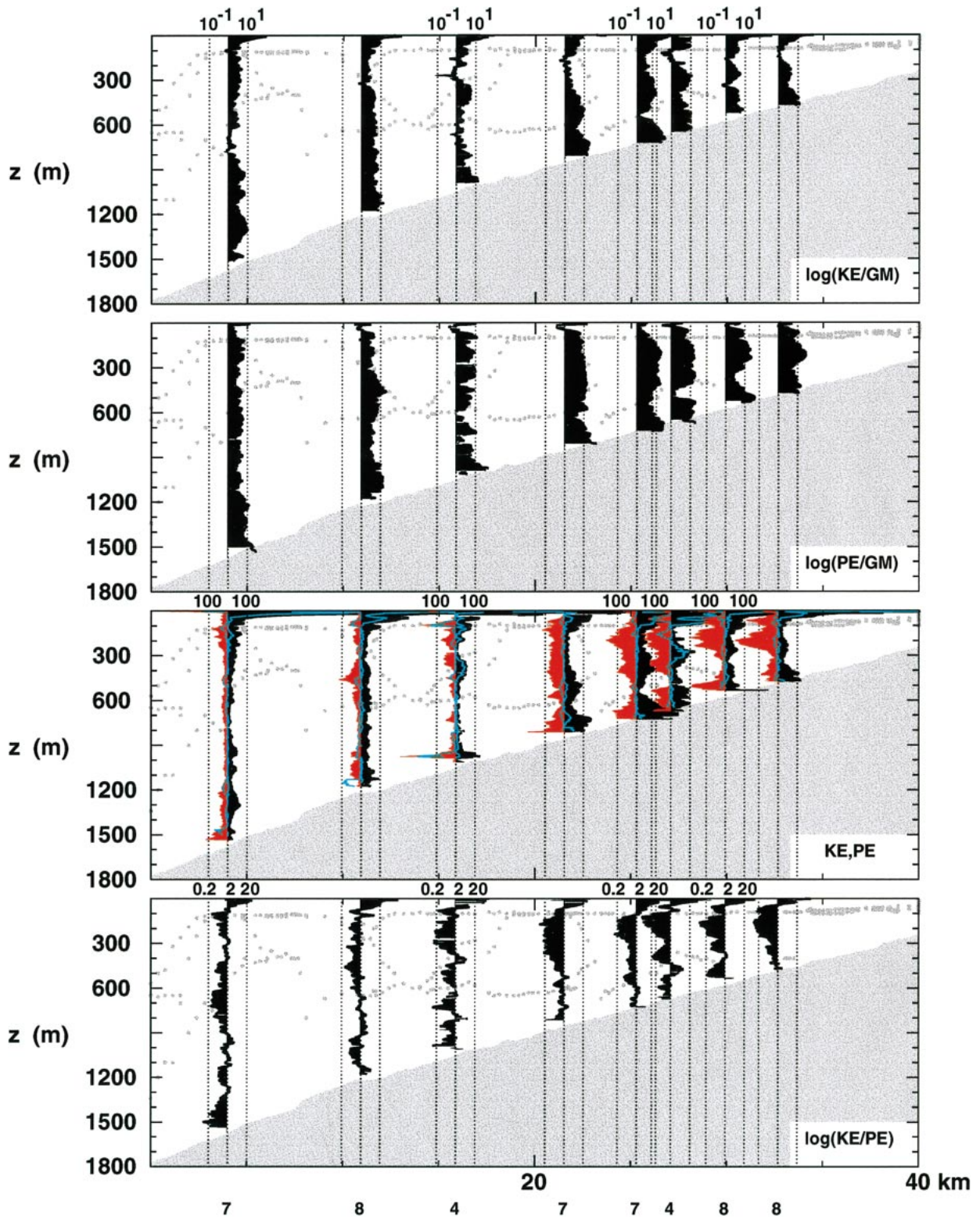


FIG. 3. Along-canyon sections of station-average (a) GM-normalized horizontal kinetic energy density $KE = (\bar{u}^2 + \bar{v}^2)/2$, (b) available potential energy density $PE = \bar{N}^2(\bar{\xi}^2)/2$, (c) dimensional energy densities in $\text{cm}^2 \text{s}^{-2}$ (black = KE, red = PE) (third panel), and (d) the log of their ratio. Numbers along the bottom axis indicate the number of profiles in each average. Turquoise curves in the third panel are energy densities in station time means. Gray dots denote the canyon rim and prominent ridges.

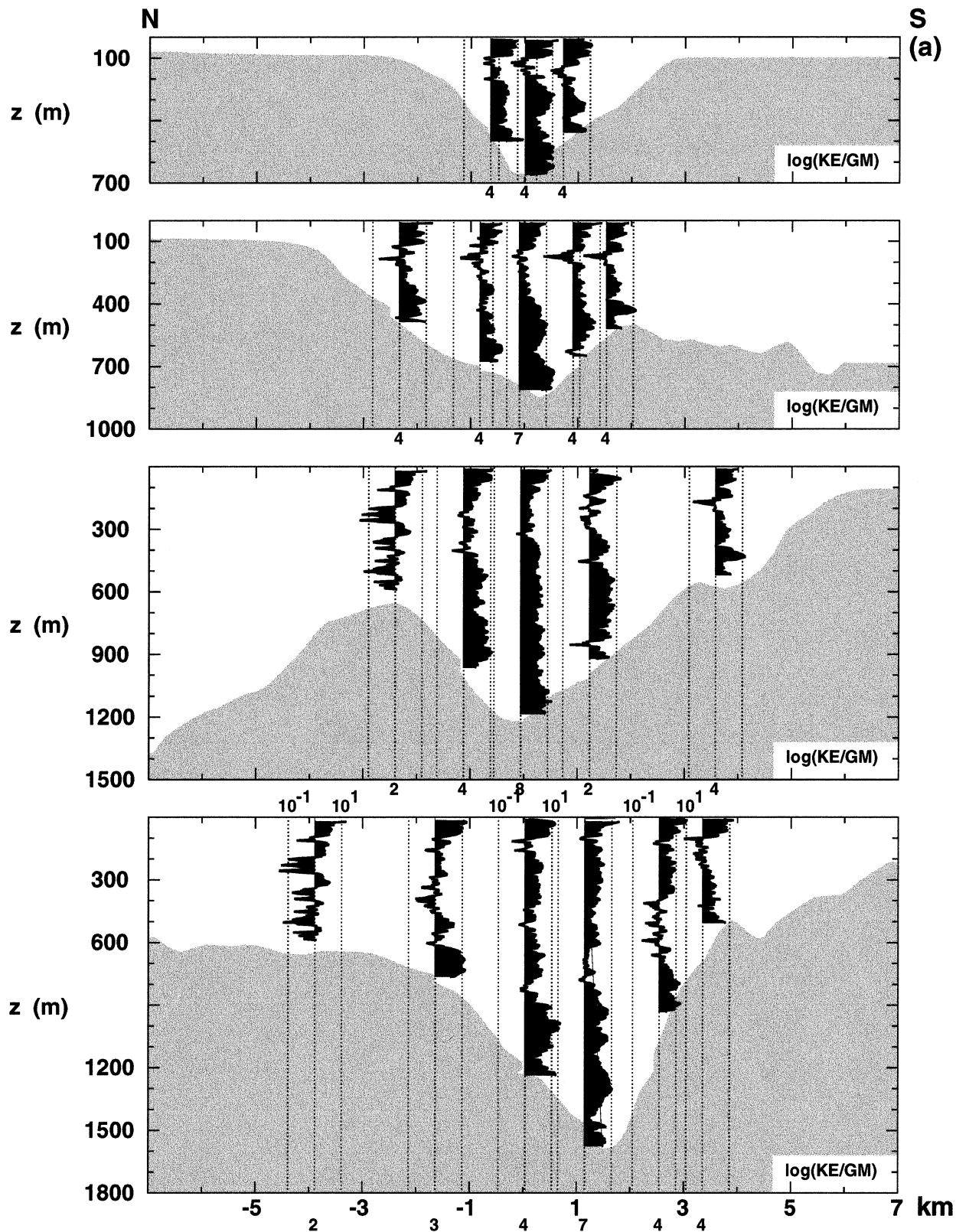


FIG. 4. Across-canyon sections of station-average (a) GM-normalized horizontal kinetic energy density KE, (b) available potential energy density PE, (c) dimensional energy densities in $cm^2 s^{-2}$ (black = KE, red = PE), and (d) the log of their ratio. Numbers along the bottom axes indicate the number of profiles in each average. Turquoise curves in (c) are energy densities in station time means.

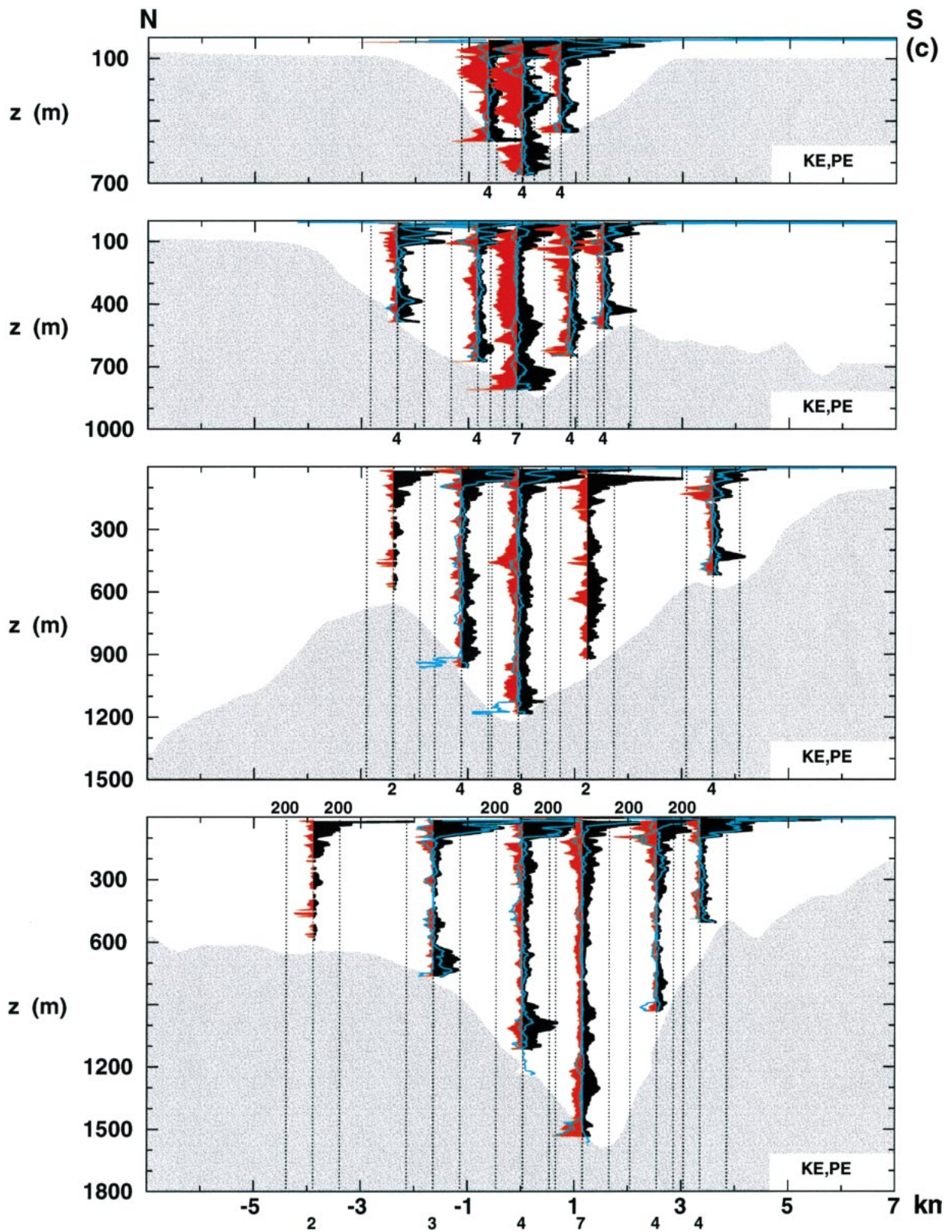


FIG. 4. (Continued)

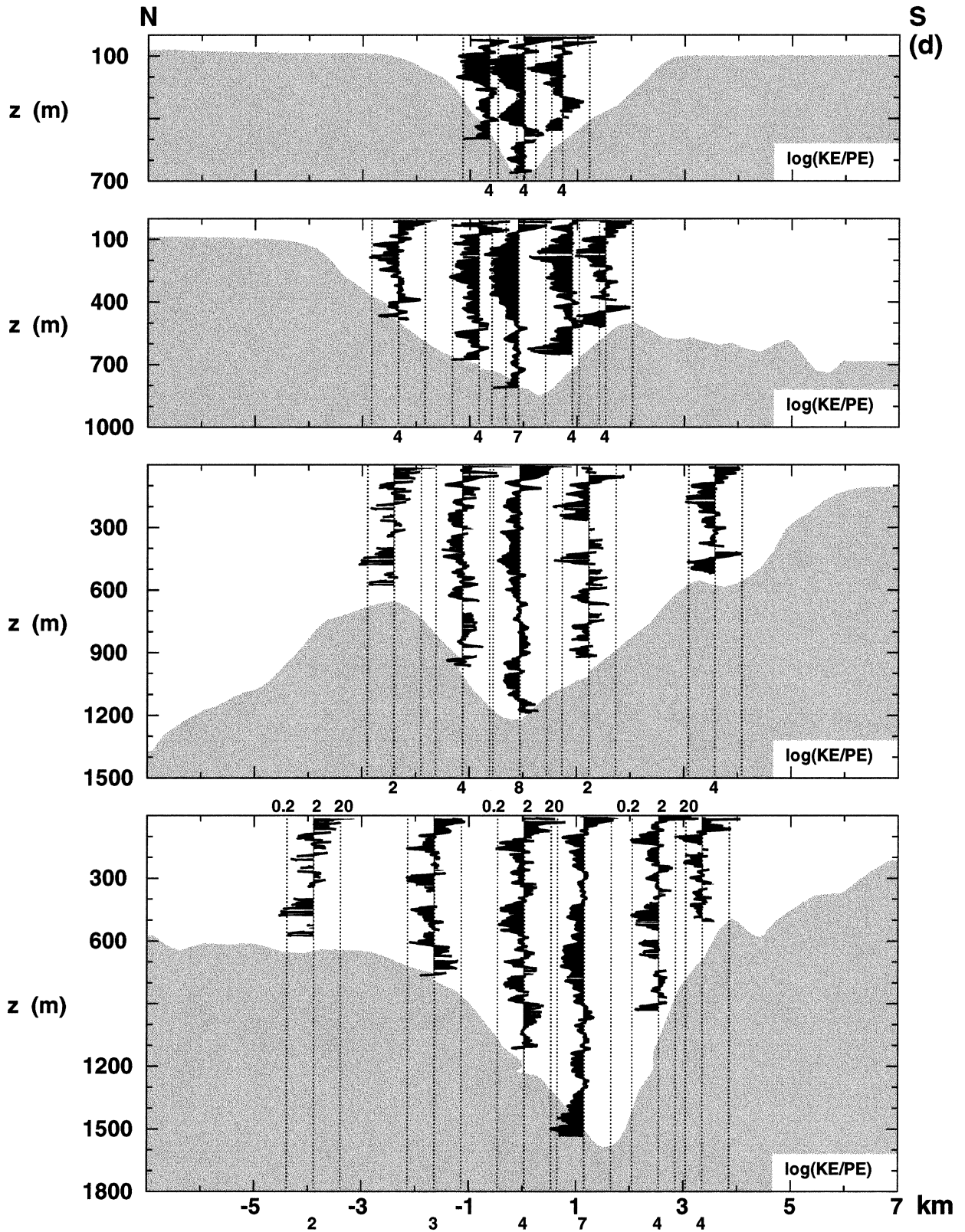


FIG. 4. (Continued)

wave band ($f < \omega < N$), the spectra resemble the $[\omega(\omega^2 - f^2)^{1/2}]^{-1}$ Garrett and Munk (GM) (1979; Cairns and Williams 1976; Munk 1981) model except for (i) the absence of a near-inertial (f) peak, (ii) a dominant semidiurnal (M_2 and S_2) peak with $150 \text{ cm}^2 \text{ s}^{-2}$ in $0.8M_2 < \omega < 1.2M_2$ corresponding to roughly half the total variance, (iii) the presence of semidiurnal and diurnal ($nM_2 + mK_1$) harmonics, and (iv) excess energy near the buoyancy frequency. The semidiurnal peak is present at all depths while its harmonics intensify toward the bottom. At subinertial frequencies, there is a diurnal (K_1 and O_1) peak that weakens away from the bottom, and a 2–3-day period peak that weakens toward the bottom. There is no break in spectral slope at the buoyancy frequency N due either to instrument noise or advective contamination (D’Asaro and Lien 2000). Spectra from the shallower (337-m isobath) broadband ADCP mooring (not shown) are higher at frequencies above M_4 , likely a signature of the tidal bores evident in the records (Rosenfeld et al. 1999; Key 1999), and show little evidence of a bottom-intensified diurnal peak. This mooring was closer to the canyon axis. Neither moorings’ measurements extended above the canyon rim so the presence or absence of an inertial peak above the canyon’s direct influence could not be confirmed.

4. Sections

This section describes along- and across-canyon spatial structure of baroclinic energy, and shear and strain variance based on the XCP–XCTD surveys. The calculation of baroclinic available potential energy $PE = \bar{N}^2 \langle \xi^2 \rangle / 2$ requires some care. Barotropic flow over a slope will uplift isopycnals, $\xi_{BT} = \mathbf{v}_{BT} \cdot (\nabla h)z / (\omega h)$ (Baines 1982), contributing to available potential energy. Kinetic-to-potential energy ratios (KE/PE) are close to one approaching the bottom if available potential energy is computed without taking this into account. Low energy ratios were also noted by Petrucio et al. (1998) and Lien and Gregg (2001), and can be inferred from the kinetic and potential energies quoted by Hotchkiss and Wunsch (1982). Petrucio et al. (1998) suggested that the low energy ratios they observed in Monterey Canyon were a result of the sidewalls suppressing the effect of rotation. Here, we argue that the barotropic tide contributes significantly to the available potential energy. To remove the barotropic contribution to the vertical displacements ξ , a linear fit with zero at the surface was subtracted ($\tilde{\xi} = \xi - \xi_z z$) from each vertical displacement profile. The average energy ratio for the residual displacement profiles $\tilde{\xi}$ was 2.06–2.10, consistent with the semidiurnal value $KE/PE = (N^2 - \omega^2)/(\omega^2 + f^2)N^2(\omega^2 - f^2) = 2.13$ (Fofonoff 1969). Barotropic bottom displacements were less than 75 m, with most less than 40 m. While there is considerable uncertainty because of the complicated topography and unknown $O(1 \text{ cm s}^{-1})$ barotropic tidal currents, these bottom dis-

placements are consistent with barotropic cross-slope flows less than 5 cm s^{-1} , with most of them consistent with flows less than 2 cm s^{-1} .

a. Baroclinic energy

For each XCP–XCTD pair, profiles of baroclinic horizontal kinetic energy density $KE = (\tilde{u}^2 + \tilde{v}^2)/2$ and available potential energy density $PE = \bar{N}^2 \tilde{\xi}^2 / 2$ were computed where \tilde{u} and \tilde{v} are the baroclinic velocities relative to depth means. Stratification $\bar{N}^2(z)$ is based on the average over all the canyon profiles. Vertical displacements $\tilde{\xi}$ had linear fits with depth subtracted to remove the barotropic contribution as just described.

Station-average profiles of baroclinic energy for the one along- and four across-canyon sections (Fig. 1) are displayed in Figs. 3 and 4, respectively. Energies are elevated compared to open-ocean (GM) values, particularly toward the head of the canyon; XCP kinetic energies are more elevated compared to GM than the factor of 2 seen in the mooring spectra (Fig. 2) because the XCP measurements were collected during spring tide while the mooring spectra are averaged over two fortnightly cycles. Toward the canyon head, KE tends to be larger near the surface and bottom, PE at middepth, consistent with dominance by mode one. Available potential energy is more enhanced than horizontal kinetic energy (upper two panels of Fig. 3, Fig. 4a, and Fig. 4b), especially along the canyon axis. Station time-mean energies (turquoise curves in Fig. 3c, Fig. 4c) are much weaker than the total energy for the most part, except near the surface where surface waves likely dominate, near the bottom where asymmetric tidal velocities (Rosenfeld et al. 1999) affect the time means, and at middepth in stations with four or fewer measurements.

As mentioned above, the canyon-wide average energy ratio (bottom panel of Fig. 3, Fig. 4d) is 2.06–2.10, commensurate with the semidiurnal 2.13 and lower than the canonical open-ocean (GM) value of 3.0. Energy ratios tend to be lower near the canyon axis, and toward the shallow end of the canyon. Higher energy ratios are found on the upper sidewalls in the deep part of the canyon. Reduced energy ratios are consistent with the absence of a near-inertial peak in the frequency spectra (Fig. 2).

b. Finescale shear and strain

While energy is dominated by large vertical scales, most of the internal-wave vertical shear $V_z = (u_z^2 + v_z^2)^{1/2}$ and strain ξ_z variance is contributed by the finescale. Variances for these quantities are estimated spectrally below. There is some question of how to interpret spectra near the bottom and surface. However, permanent well-mixed surface and bottom boundary layers were at most a few meters thick so the water column is well stratified and able to support internal waves near both boundaries. Bottom-trapped topographic waves

(Rhines 1970) may also contribute to shear and strain variance near the bottom—recall diurnal motions were bottom intensified (Fig. 2).

For the spectral estimates, half-overlapping profile segments 128 m long were Fourier transformed. Gradient Froude number V_z/\overline{N} and strain ξ_z spectra, corrected for data smoothing and interpolation, are displayed in Fig. 5. In Fig. 5a, periodograms with similar Froude number variance were bin averaged together. At low wavenumber ($\lambda_z \sim 100$ m), the resulting bin-averaged Froude spectra (solid curves) span over an order of magnitude from half to 10 times GM. Froude spectra steepen with increasing spectral level so that the high-wavenumber end ($\lambda_z \sim 15$ m) spans less than a factor of three. The corresponding strain spectra (dotted curves) show less variability and are steeper than the Froude spectra such that the shear/strain (energy) ratio is smaller at low than at high wavenumbers.

In Fig. 5b, periodograms with similar strain variance were bin averaged together. The strain spectra span almost two orders of magnitude at low wavenumber. They are slightly blue for GM levels but steepen toward k_z^{-1} for higher spectral levels. The corresponding Froude spectra are more or less flat and indistinguishable for all strain variances. Comparison of Figs. 5a and 5b suggests that shear and strain levels do not covary in the canyon.

Station-average alongcanyon (Fig. 6) and across-canyon (Fig. 7) sections of GM-normalized shear and strain variance as deduced from the spectra are elevated compared to open-ocean (GM) values, particularly near the bottom. Strain is more elevated than shear (second panel of Fig. 6, Fig. 7b). Enhancement of strain variance by an order of magnitude is found below 300–500-m depth at most stations. Though strains below 900-m depth at the two deepest axis stations (Fig. 6), and on the axis and its immediate neighbor to the left in the two across-canyon sections (bottom two panels of Fig. 7b), are contaminated by instrument noise, elevated strains elsewhere are well above the noise.

The finescale analog to the energy ratio, the shear-strain ratio $R_\omega = V_z^2/(\overline{N}^2\xi_z^2)$, is close to the semidiurnal value of 2.13 in the shallow profiles and in the upper water column of the deeper profiles (bottom panel of Fig. 6, Fig. 7c) but less than 1 near the bottom in some of the deeper stations where temperature noise amplified by weak mean stratification dominates the strain signal.

5. Parameterizations of turbulent diffusion

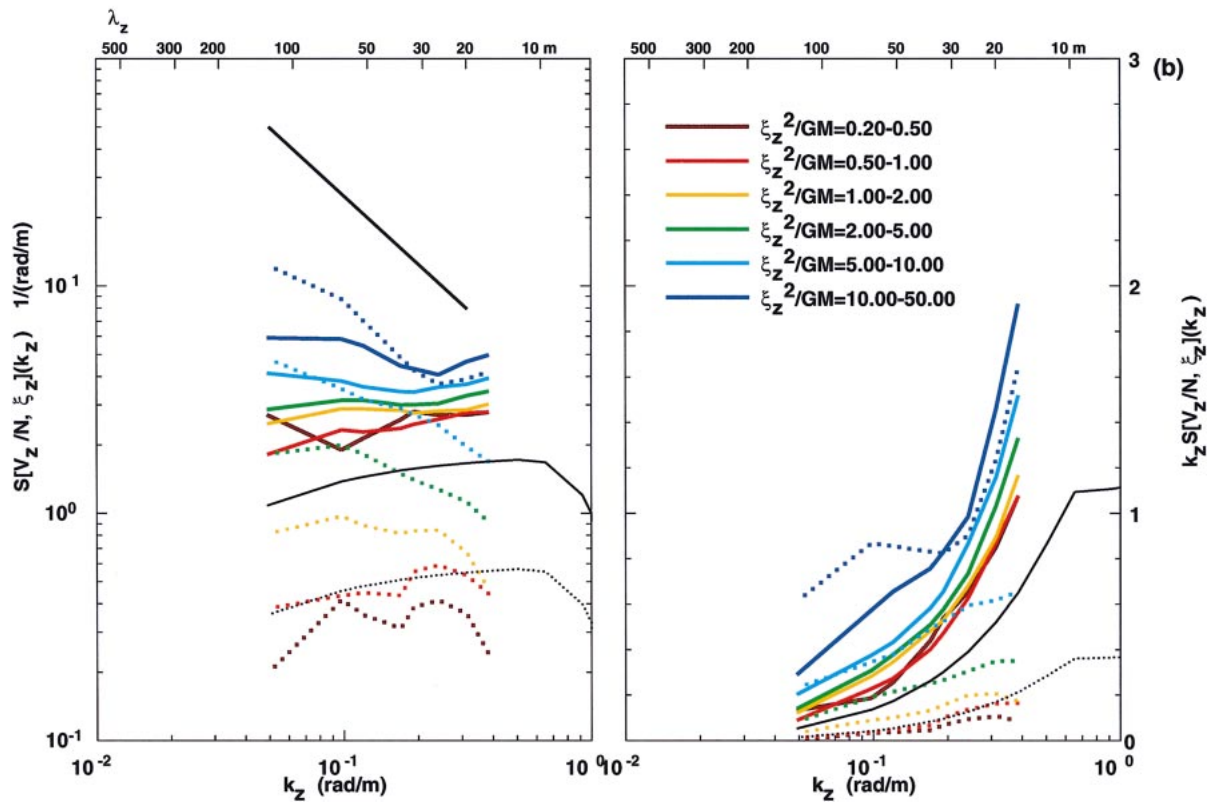
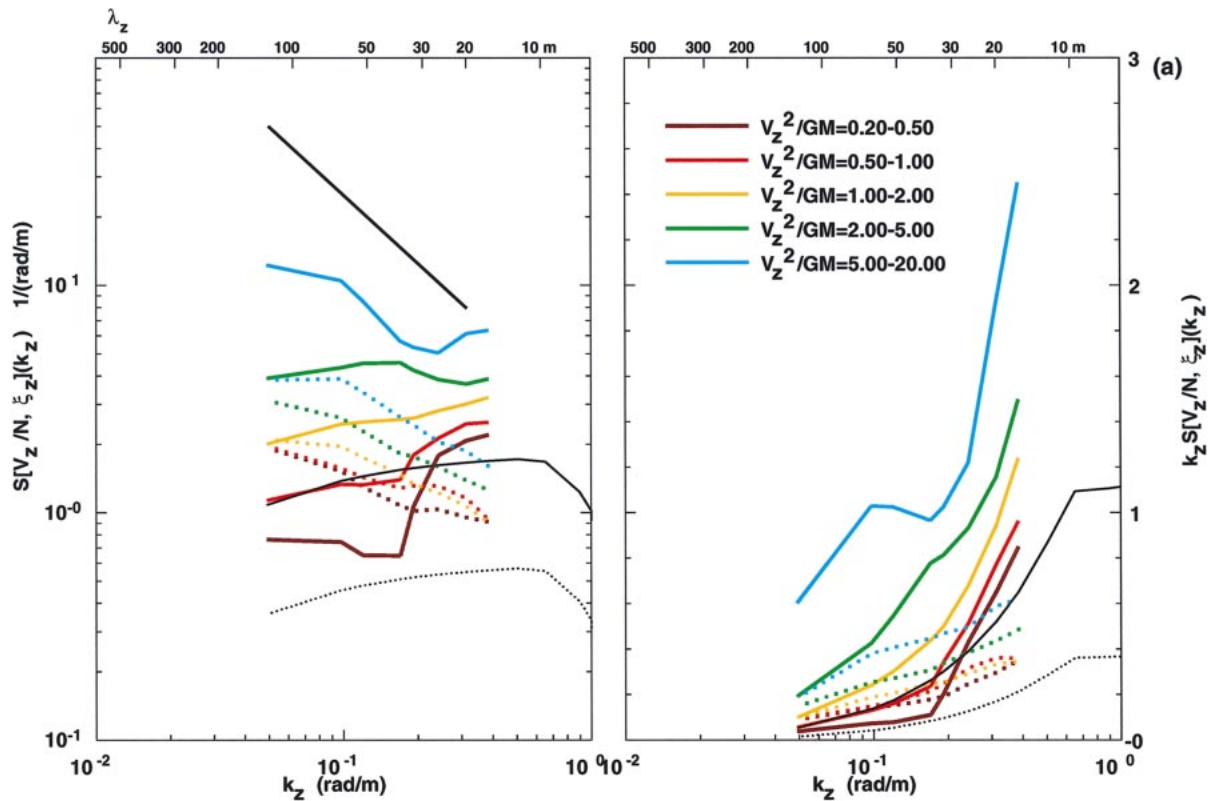
Four finescale parameterizations for the turbulent kinetic energy dissipation rate ϵ and eddy diffusivity K as a function of finescale shear and strain variance have emerged in the past decade (appendix). These take the form $K\alpha E^2$ based on hydrostatic internal wave–wave interaction theories (McComas and Müller 1981; Henney et al. 1986) for wave fields described by the Garrett and Munk model (Cairns and Williams 1976; Munk

1981; Gregg and Kunze 1991), where E is the level of the internal wave–band vertical wavenumber spectra. The first parameterization (Gregg 1989) uses shear only. Subsequent iterations used strain only (Wijesekera et al. 1993), then shear and strain together (Polzin et al. 1995; Sun and Kunze 1999) to account for non-GM ocean frequency spectra. The parameterizations imply that elevated turbulent mixing requires elevated internal wave spectral levels. They have been used to infer turbulent mixing rates in the stratified deep ocean interior (Gregg and Kunze 1991; D’Asaro and Morison 1992; Kunze et al. 1992; Duda and Jacobs 1995; Kunze and Sanford 1996; Polzin and Firing 1997).

Variances from the 128-m spectra were used as input for the four parameterizations (appendix). To obtain variances, the shear spectra $S[V_z](k_z)$ were integrated from their lowest resolved wavenumber ($\lambda_z = 128$ m) to an upperbound wavenumber corresponding to variance $0.7\overline{N}^2$ or to $\lambda_z = 32$ m, whichever came first, following Kunze et al. (1992), Polzin et al. (1995), and Kunze and Sanford (1996); strain and normalizing GM variances were computed over the same wavenumber band. This includes only four spectral points. Inferred diffusivities from the four parameterizations are scatterplotted against each other in Fig. 8. Since the shear–strain ratio must exceed 1.0 for hydrostatic internal waves, the shear-and-strain parameterizations are unable to cope with occurrences of shear–strain ratio less than one (triangles in Fig. 8). Shear–strain ratios of 1.01 were substituted.

The shear-only (Gregg 1989) and strain-only (Wijesekera et al. 1993) diffusivities have similar averages to within a factor of three ($\langle K \rangle = 0.2 \times 10^{-4} \text{ m}^2 \text{ s}^{-1}$) but show no relation to one another (upper-left panel), forming a diffuse cloud of points. This is consistent with the lack of correlation between the shear and strain spectra (Fig. 5). This conclusion is unchanged when suspect strain data from below 900-m depth, near the bottom and near the surface are excluded from the statistics. The shear-and-strain parameterized diffusivities are correlated with the shear-only diffusivities (upper right, lower left) for higher shear–strain ratios (dots) but predict higher diffusivities when strain is elevated (triangles). The Polzin et al. and upper-limit Sun and Kunze diffusivities are well correlated with averages $\langle K \rangle = 0.6 \times 10^{-4} \text{ m}^2 \text{ s}^{-1}$ to within a factor of three. Because the Polzin et al. parameterization has been validated against microstructure measurements in the open ocean, it will be used in subsequent comparisons with microstructure.

At the shallow end of the canyon, where fine- and microstructure measurements overlap (Fig. 9), the turbulent dissipation rate parameterization of Polzin et al. (1995) underestimates microstructure values by a factor of 30. (Note that diffusivities in Fig. 9 are higher than the surveywide average in Fig. 8 because Fig. 8 includes all the profiles, not just the elevated canyon axis values.) Average microstructure dissipation rates along the can-



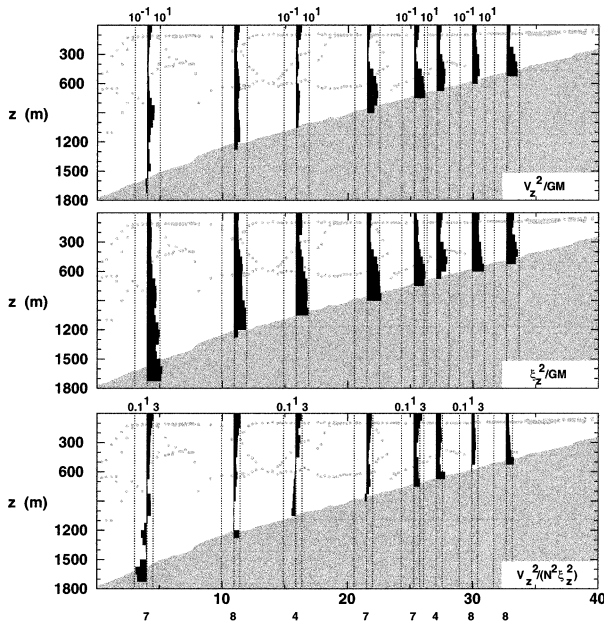


FIG. 6. Along-canyon sections of GM-normalized (top) shear variance V_z^2 , (middle) strain variance ξ_z^2 , and (bottom) shear-strain ratio $V_z^2/(\overline{N^2 \xi_z^2})$. Gray dots denote the canyon rim and prominent ridges. Variances were based on integrating spectra from half-overlapping 128-m long profile segments over vertical wavelengths $\lambda_z = 32$ –128 m, then averaging over station occupations. (top) Shear variance exceeds the GM value throughout the canyon and by almost an order of magnitude in the bottom 300 m at the shallow end of the canyon. (middle) Strain variance is even more elevated; values below 900 m in the two deepest stations are contaminated by instrument noise. (bottom) Shear-strain ratios are close to the semidiurnal internal wave value of 2.13 except near the bottom in the deeper stations.

yon axis during the spring tide are $\langle \epsilon \rangle = (700\text{--}8000) \times 10^{-9} \text{ W kg}^{-1}$, corresponding to eddy diffusivities $\langle K \rangle = (40\text{--}700) \times 10^{-4} \text{ m}^2 \text{ s}^{-1}$, with no obvious dependence on along-axis position; neap dissipation rates were two orders of magnitude smaller (CG). These values are three orders of magnitude larger than typical open-ocean values (Gregg 1989; Ledwell et al. 1993; Toole et al. 1994; Kunze and Sanford 1996). By comparison, Lien and Gregg (2001), MacKinnon and Gregg (2001, manuscript submitted to *J. Phys. Oceanogr.*), and CG report $\langle \epsilon \rangle \sim 20 \times 10^{-9} \text{ W kg}^{-1}$ and $\langle K \rangle \sim 10^{-4} \text{ m}^2 \text{ s}^{-1}$ on stratified continental shelves. Nash and Moum (2001) found hydraulically driven turbulent diffusivities of $170 \times 10^{-4} \text{ m}^2 \text{ s}^{-1}$ over a bank. Previous microstructure measurements on the south canyon wall near axis depths of 600 m (Lueck and Osborn 1985) revealed a 170-m

thick stratified turbulent bottom boundary layer with dissipation rates $\epsilon = (70\text{--}500) \times 10^{-9} \text{ W kg}^{-1}$ and average eddy diffusivities of $15 \times 10^{-4} \text{ m}^2 \text{ s}^{-1}$. The Lueck and Osborn values are also over an order of magnitude higher than those inferred from finescale parameterizations in the vicinity of their site. Thus, the finescale parameterizations underestimate turbulence by at least an order of magnitude at the shallow end of Monterey Canyon. Microstructure measurements to 600-m depth along the canyon axis at the canyon mouth (not shown) are more comparable to open-ocean values and finescale parameterized estimates. Underestimation by the finescale parameterizations may arise because either (i) the methodology used here for the parameterizations is flawed, or (ii) mechanisms in the canyon transfer energy toward small scales and turbulence production more rapidly than in the open ocean. These two possibilities are discussed in turn below.

First, the approach used here may underestimate the shear and strain variance. To reiterate, half-overlapping 128-m profile segments were Fourier-transformed and the resulting shear spectra integrated to an upper-bound wavenumber $k_z = 0.2 \text{ rad m}^{-1}$ corresponding to a vertical wavelength $\lambda_z = 32 \text{ m}$, or where the shear variance approached $0.7\overline{N^2}$, whichever came first (usually this was 0.2 rad m^{-1}). One concern is that these segments may be too short to capture the finescale shear spectral level (Gargett 1990). If the parameterizations $K\alpha E^2$ are valid, microstructure diffusivities 1000 times open-ocean values of $0.1 \times 10^{-4} \text{ m}^2 \text{ s}^{-1}$ should imply internal wave spectral levels E that are 30 times open-ocean (GM) values. Atmospheric (Smith et al. 1987) and oceanic (Duda and Cox 1989; Gregg et al. 1993) vertical wavenumber spectra (see Fig. 5) suggest that the cutoff vertical wavenumber k_c associated with finescale steepening of the shear spectral slope from flat at low wavenumbers to k_z^{-1} (Gargett et al. 1981) behaves roughly as $Ek_c = \text{constant}$. For a GM level spectra, the corresponding vertical wavelength is $\lambda_c = 10 \text{ m}$ so spectral levels 30 times GM imply $\lambda_c = 300 \text{ m}$! Consistent with this, the spectral slopes steepen with increasing variance in Fig. 5. This suggests that the 128-m profile segments used for Figs. 6–8 may be too short to resolve shear variance from wavelengths larger than the cutoff. However, using 512-m segments did not alter the results. While 512-m also may be too short to resolve the shear variance, longer segments will not fit into the water depth in most of the canyon profiles. Therefore, the

FIG. 5. Vertical wavenumber spectra for gradient Froude number V_z/\overline{N} (solid) and strain ξ_z (dot) in (left) log-log and (right) variance-preserving formats. Black solid and dotted curves are GM model Froude number and strain spectra, respectively. The diagonal black line corresponds to a -1 slope. (a) Periodograms containing the same shear variance have been bin averaged. The lowest bin contains shear variance (0.2–0.5) GM and the highest (5–20) GM. The Froude spectra steepen with increasing spectral level. There is little spread in the strain spectra. (b) Periodograms of the same strain variance have been bin averaged. The resulting strain spectra steepen with increasing spectral level. In this case, there is little spread of the shear spectra. Together, (a) and (b) suggest that shear and strain variances do not covary.

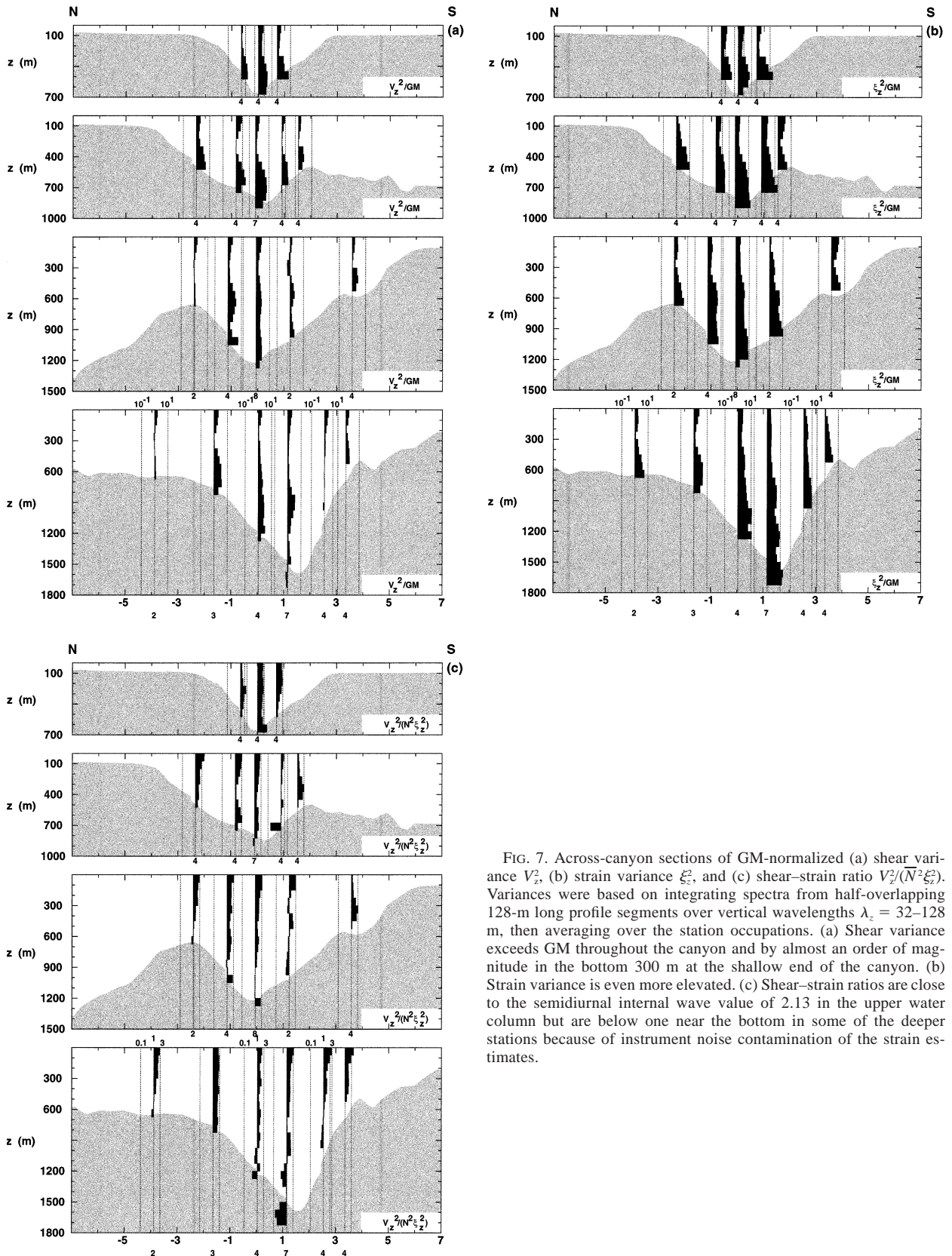


FIG. 7. Across-canyon sections of GM-normalized (a) shear variance V_z^2 , (b) strain variance ξ_z^2 , and (c) shear-strain ratio $V_z^2/(N^2\xi_z^2)$. Variances were based on integrating spectra from half-overlapping 128-m long profile segments over vertical wavelengths $\lambda_z = 32\text{--}128$ m, then averaging over the station occupations. (a) Shear variance exceeds GM throughout the canyon and by almost an order of magnitude in the bottom 300 m at the shallow end of the canyon. (b) Strain variance is even more elevated. (c) Shear-strain ratios are close to the semidiurnal internal wave value of 2.13 in the upper water column but are below one near the bottom in some of the deeper stations because of instrument noise contamination of the strain estimates.

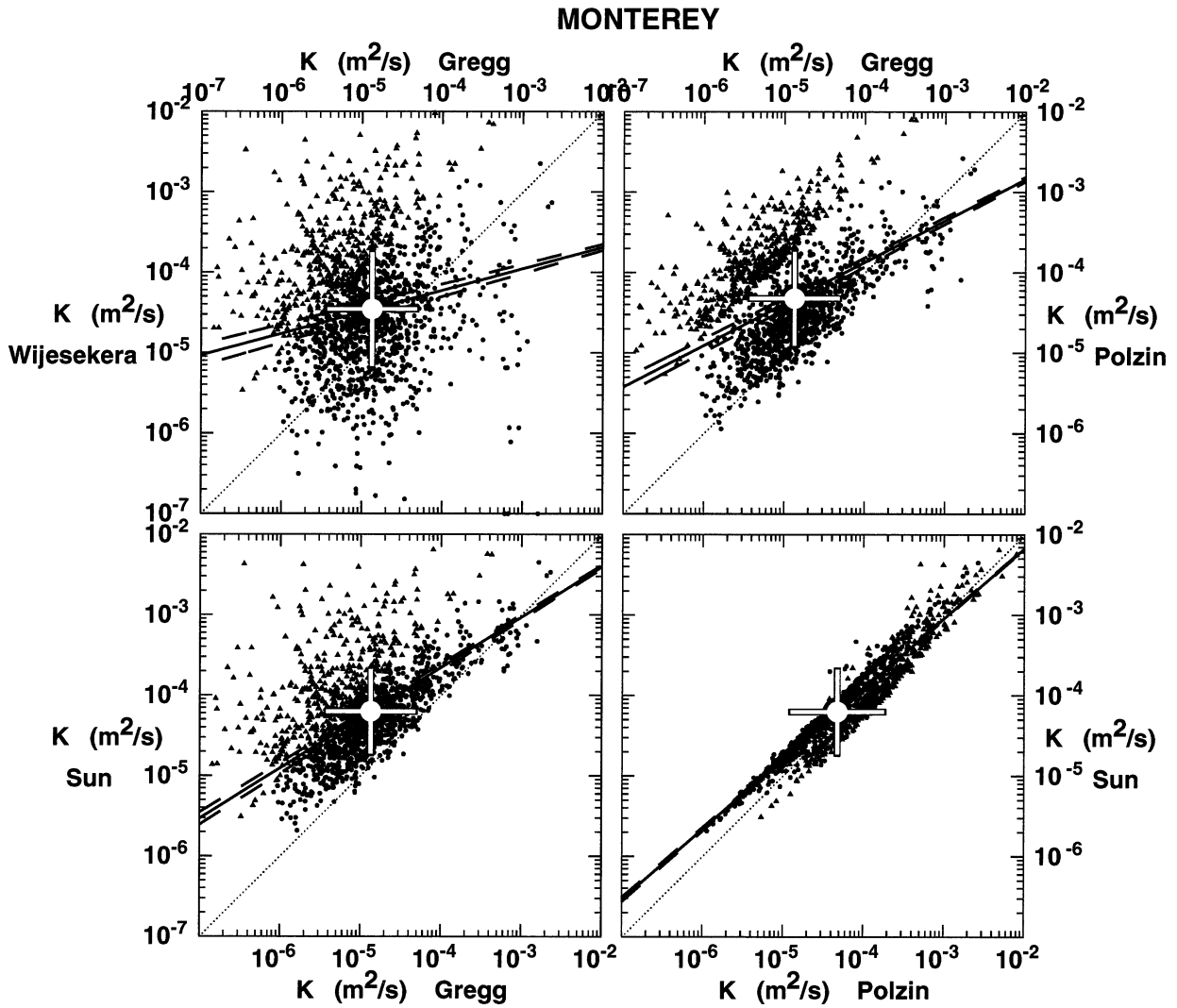


FIG. 8. Scatterplots of turbulent eddy diffusivity inferred from four parameterizations (appendix) using finescale spectral shear and strain variances from overlapping 128-m profile segments. Dots correspond to shear/strain ratios greater than one, triangles to shear/strain ratios less than one. The cross in each panel shows the mean eddy diffusivities with standard deviations. Solid and dashed lines are least squares linear fits and standard deviations, respectively. (upper-left) Shear-only (Gregg 1989) and strain-only (Wijesekera et al. 1993) parameterizations reveal no correlation between shear and strain variances. Compared to Gregg's shear-only parameterization, the two shear-and-strain parameterizations (Polzin et al. 1995; Sun and Kunze 1999) are elevated due to excess strain in the canyon. The shear-and-strain parameterizations are consistent with each other (upper right, lower left).

k_z^{-1} regime may fill the water column in much of the canyon (see Fig. 5) so that there is no wavenumber band corresponding to weakly nonlinear internal waves (D'Asaro and Lien 2000).

Gregg (1989) originally used 10-m first-difference shears in his parameterization. This scale is likely too small for the reasons given above (Gargett 1990). However, first-difference shear and strain estimates over 20-, 50-, 100-, and 200-m intervals normalized by GM variances derived in the same way were in close agreement with each other and with the 128-m spectral estimates. We conclude that turbulence in a canyon is produced in a fundamentally different manner than in the open ocean.

Interactions within the canyon internal wave field

may transfer energy from large to small vertical scales more rapidly than in the open ocean, enhancing turbulence production. The open-ocean parameterizations are based on a hydrostatic GM model spectrum, while the canyon internal wave field is decidedly non-GM, having no near-inertial waves, dominance by semidiurnal fluctuations (and their harmonics, Fig. 2), and tidal bores near the bottom (Rosenfeld et al. 1999; Key 1999).

Interactions with canyon topography may transfer energy to small scales more efficiently than wave-wave interactions. These interactions may include (i) internal wave critical reflection (Eriksen 1982), (ii) scattering of the barotropic tide and internal waves off small-scale topography (Baines 1973, 1982; Bell 1975; Craig 1987;

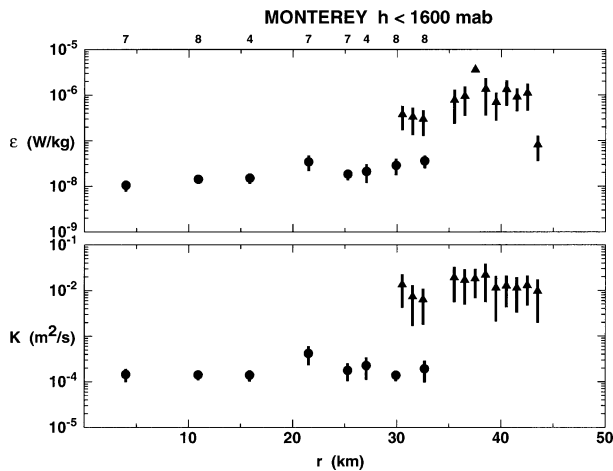


FIG. 9. (top) Depth-averaged turbulent dissipation rates ϵ and (bottom) eddy diffusivities K along the canyon axis. Large dots are inferences from the Polzin et al. finescale parameterization (Fig. 8), triangles at the shallow end ($r > 30$ km) are direct microstructure estimates. Over the range where the measurements overlap, microstructure diffusivities are $(30\text{--}700) \times 10^{-4} \text{ m}^2 \text{ s}^{-1}$, a factor of 30 larger than values inferred from the finescale parameterizations.

Thorpe 2001; St. Laurent and Garrett 2002, hereafter SG), (iii) internal lee wave generation by smallscale topography (Bell 1975; Thorpe 1996), and (iv) eddy shedding (MacCready and Pawlak 2001). Bottom slopes near critical at the semidiurnal frequency are found throughout the bay's continental shelf, on the rim, between the 800- and 2000-m isobath of the submarine fan north of the canyon mouth, and along the canyon axis (see Fig. 10). Canyon walls are much steeper. The Baines (1982) forcing function $\nabla^2(1/h)$ is strongest along the canyon rim and at the shelf break. It is also large inshore throughout Monterey Bay because of the shallowness of the water.

6. Energy fluxes

While there is some uncertainty about the definition of along canyon because of the many twists and turns in the canyon axis, station-average vertically integrated horizontal energy fluxes $\langle \bar{v}\bar{p} \rangle_\phi dz$ appear to be steered by the sinuous canyon topography (Fig. 10). Uncertainties in these flux estimates are difficult to evaluate as only a single tidal cycle was sampled and fluxes naturally fluctuate between zero and their maximum as $\cos^2(\omega t)$. Comparison with fluxes from neighboring deep cross-canyon stations suggest uncertainties of at most 20%. In Fig. 10, the pressure anomaly was calculated from the full displacement profile without removing the barotropic contribution (section 4) so the full energy flux is represented, not just the internal wave contribution. Removing the barotropic displacement profile reduces fluxes at the deepest cross-canyon section across the mouth and at the shallowest station (not

shown), possibly indicating internal tide sources at these sites, but elsewhere changes the fluxes little.

Fluxes are upcanyon and about 5 kW m^{-1} at the mouth, diminishing to $O(1 \text{ kW m}^{-1})$ toward the shallow end and even reversing at the shallowest station (Fig. 10). Correlations $|\bar{v}\bar{p}|/(\sqrt{\bar{v}} \cdot \sqrt{\bar{p}})$ typically exceed two thirds in profiles with vertically integrated fluxes greater than 1 kW m^{-1} , indicating that the bulk of the variance is participating in the upcanyon flux. The fluxes are large compared to $O(0.1 \text{ kW m}^{-1})$ estimates of across-slope internal tidal fluxes elsewhere (Torgrison and Hickey 1979; Holloway 1984, 1996; Sherwin 1988; Garcia Lafuente et al. 1999).

The decrease in upcanyon energy flux toward the shallow end of the canyon is not monotonic. There is little change between the two deepest axis stations, despite a sharp bend in the axis between them, while there is a dramatic drop at the next axis station, then an increase, followed by another increase, then comparable fluxes until the shallowest axis station where the vertically integrated flux is downcanyon. Flux magnitudes are generally weaker off axis. The shallow fluxes of 1 kW m^{-1} are consistent with Petrucio et al.'s (1998) inferences based on plugging vertical and horizontal wavelength estimates into the group velocity relation $C_g E$.

Flux orientation is roughly independent of depth (Fig. 11) at most axis stations with exceptions near the bottom. At the deep end of the canyon, energy fluxes are directed upcanyon at all depths while, in the shallower reaches of the canyon, energy fluxes are upcanyon in the upper water column and downcanyon near the bottom. In the vertical plane, flux vectors are either parallel to semidiurnal ray paths (solid and dotted curves in the top panel of Fig. 11b), or flatter as might be expected for a superposition of up- and downgoing waves. Near-bottom fluxes in the deep profiles are parallel to the bottom slope (Fig. 11b). Flux magnitudes exhibit minima at middepth, consistent with dominance by low modes. While Sherwin and Taylor (1990), Holloway (1996), and Garcia Lafuente et al. (1999) found energy fluxing onshore at depth and offshore near the surface, their results may have been biased by failing to ensure that the depth-average pressure anomaly vanishes in their calculations (section 2c).

No obvious source for the influx at the mouth can be identified in Fig. 10. Assuming that the fluxes could not negotiate sharp bends in the canyon, Petrucio et al. (1998) speculated that either the sharp ridge at $36^\circ 45' \text{ N}$, $122^\circ 3' \text{ W}$ or the submarine fan (their smooth ridge) at $35^\circ 48' \text{ N}$, $122^\circ 10' \text{ W}$ could be the source of upcanyon energy fluxes they found at the shallow end. Fluxes do not appear to be radiating toward the canyon from either feature (Fig. 10)—though it is possible that internal tides are being generated at the base of the submarine fan facing the canyon mouth at unsampled depths below 1600 m. Fluxes appear to have no difficulty negotiating the deepest bend in the canyon axis (Fig. 10) so that it

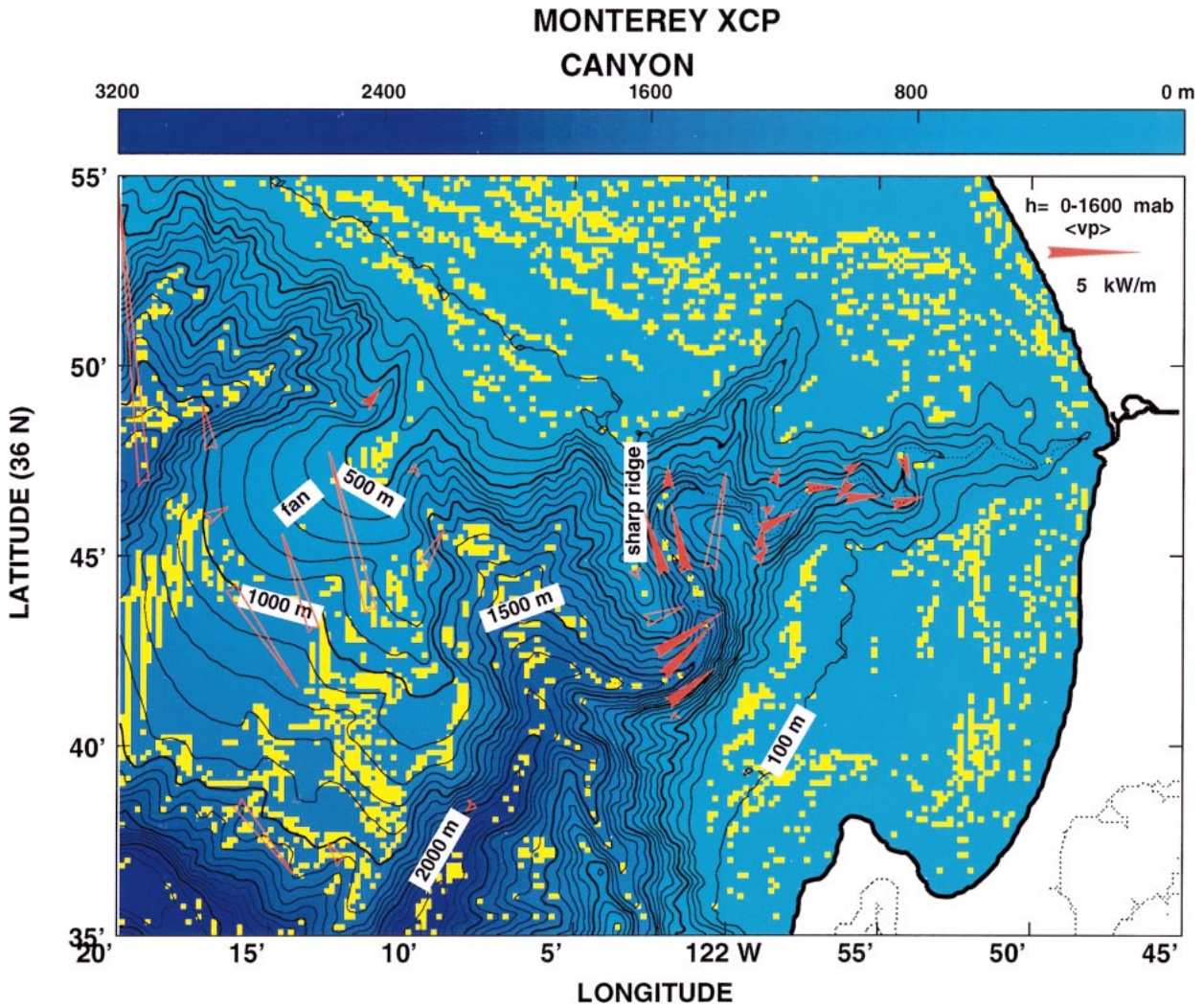


FIG. 10. Depth-integrated station-average horizontal energy fluxes $\int \langle \bar{v}\bar{p} \rangle_{\omega} dz$ (red arrows). Solid arrows are based on four or more profile pairs, so represent a reasonable average over a semidiurnal cycle while open arrows are based on less than four profile pairs and are less reliable. In the canyon, fluxes appear to be steered upcanyon by topography (with the exception of downcanyon fluxes at the shallowest station), diminishing from about 5 kW m^{-1} at the mouth to $\pm 1 \text{ kW m}^{-1}$ toward the head. Fluxes tend to be weaker off axis. On the submarine fan to the north of the canyon mouth, fluxes are largely alongslope to the NNW or SSE, and appear to be directed away from sites of near-critical bottom slope for semidiurnal frequencies (yellow patches). Submarine fan fluxes are based on single XCP-XCTD pairs so may not be representative. Bottom slopes were calculated over the $250 \text{ m} \times 250 \text{ m}$ grid spacing. Near-critical slopes are found over the shelf, on the flanks of the submarine fan, and along the canyon axis.

may be possible for internal tides generated deeper along the canyon axis to propagate all the way to the canyon head; canyon walls are sufficiently steep that internal tides should reflect from them as from a vertical wall. On the other hand, fluxes weaken dramatically at the second deepest bend (Fig. 10), signifying an energy sink. Upcanyon fluxes pick up again farther up canyon, suggesting local generation by scattering of the surface tide from canyon topography (Prinsenber and Rattray 1975; Baines 1982; Craig 1987). Local sources are also indicated by the downcanyon flux at the shallowest station. Thus, both sources and sinks for internal tide energy seem to be present along the canyon axis.

Over the submarine fan to the north of the canyon mouth, stronger and more variable fluxes are found than in the canyon (open arrows in Fig. 10). However, these estimates are based on single XCP-XCTD pairs so have not been averaged over a tidal cycle. Thus, these estimates may range from zero to their maximum value as $\cos^2(\omega t)$ in the direction of propagation, and fluctuate around zero in the orthogonal direction as $\cos(\omega t) \sin(\omega t)$. Moreover, the California Undercurrent is a potential source of contamination in many of the profiles. Nevertheless, some general trends are evident. Slope fluxes tend to run northwest or southeast, parallel to (i) the continental slope and (ii) the surface tide's propa-

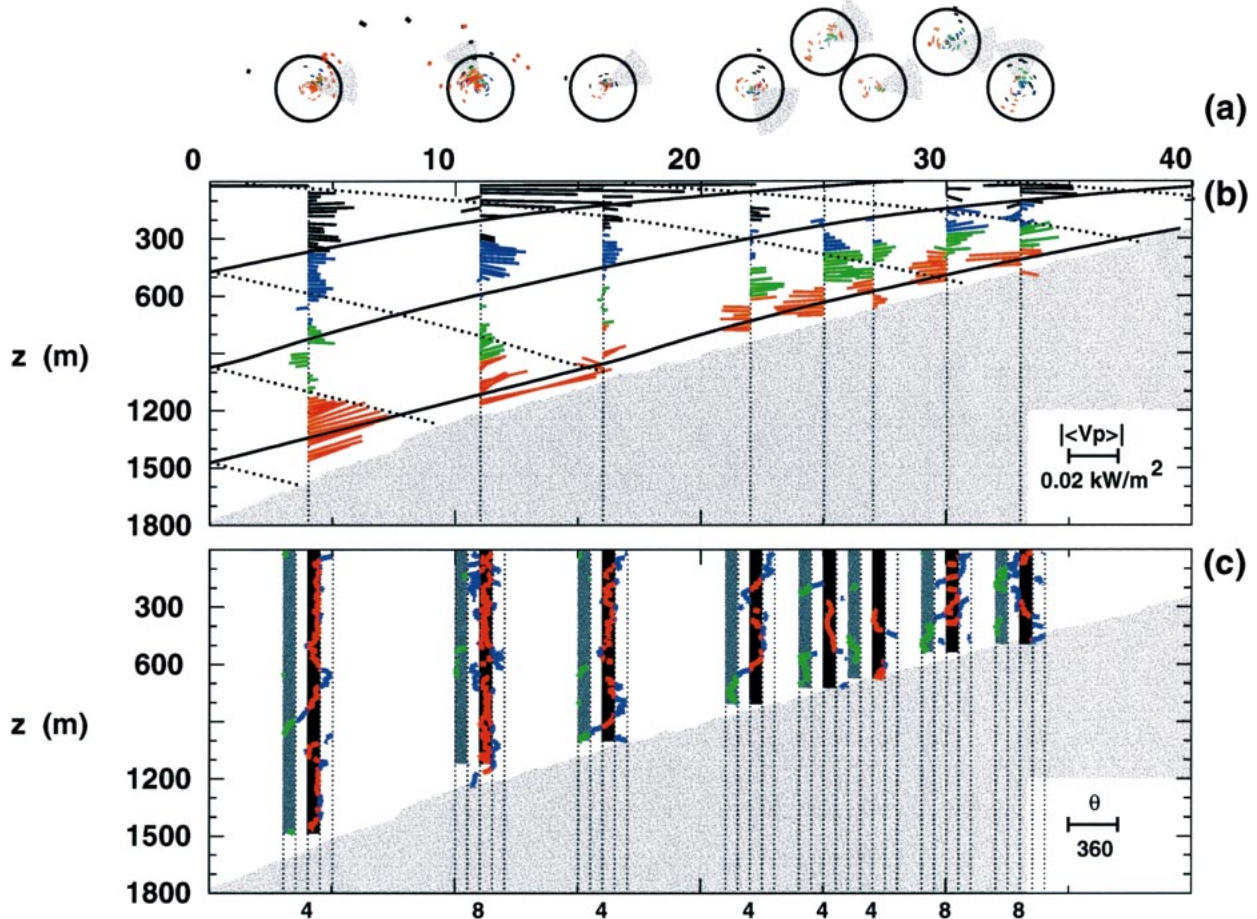


FIG. 11. Along-axis profiles of station-average energy flux $\langle \tilde{v}\tilde{p} \rangle_\phi$ based on semidiurnal fits to velocity, pressure, and vertical displacement (from which vertical velocity is deduced). (a) Compass roses are color-coded for fractional depth (black, blue, green, and red for successive quarters of the water column) with 0.05 kW m^{-2} diameter circles and gray wedges indicating the range of canyon axis orientation. (b) Profiles of along-axis energy flux are plotted only if they lie within $\pm 45^\circ$ of the upaxis (plotted positive) or downaxis (plotted negative) directions and are also color-coded by depth. Solid and dotted black curves denote semidiurnal ray paths. (c) Energy-flux orientations θ relative to the canyon axis direction are only plotted if the flux magnitude exceeds 0.001 kW m^{-2} . Dotted vertical lines separate quadrants. Black vertical bars indicate the quadrant corresponding to upcanyon orientation (red flux orientation), gray vertical bars the quadrant corresponding to downcanyon orientation (green flux orientation). Flux orientations neither up- nor downcanyon are blue. Most flux orientations are parallel to the canyon axis and are upcanyon except for downcanyon orientations in the bottom 300 m at the shallow end of the canyon. Numbers along the bottom axis indicate the number of profiles going into each average. At the second deepest and two shallowest stations, orientations are similar for the two occupations on successive days.

gation up the coast. Fluxes are largest in the upper and bottom 300 m, and appear to be directed away from regions where the bottom slope is near critical for the semidiurnal frequency (yellow patches); for example, the $\sim 15 \text{ kW m}^{-1}$ northward energy flux on the northwest flank of the fan (westernmost hollow arrow) can be traced to near-critical slopes due south on the west flank. The fluxes show no relation to the Baines forcing function (not shown). Fluxes may also arise from scattering of the surface tide from smallscale topographic features (Bell 1975). In contrast, Thorpe (1996) finds that internal lee waves generated by a mean flow over an undulating continental slope tend to propagate up-slope.

7. The energy balance

The energy flux $\langle \tilde{\mathbf{v}}\tilde{p} \rangle_\phi$ and turbulent dissipation rate ϵ estimates can be used to test the hypothesis that internal tides entering the canyon mouth lose their energy to turbulence as they propagate toward the head of the canyon in an internal surf. In support of this idea, depth-integrated energy fluxes are steered upcanyon and diminish toward the head of the canyon (Fig. 10). Petrucio et al. (1998) used the energy-flux difference between their two stations to infer turbulence production rates of $10^{-6} \text{ W kg}^{-1}$, consistent with the microstructure estimates (Fig. 9). Mathematically, the hypothesis can be expressed from conservation of energy assuming

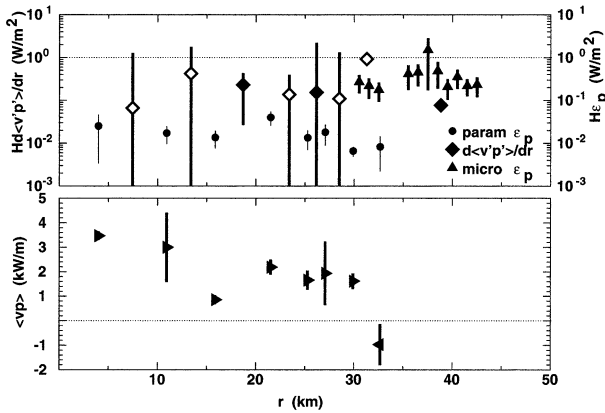


FIG. 12. (top) A test of the hypothesis that turbulence production ϵ_p along the canyon axis arises from alongcanyon convergence of upcanyon energy fluxes (2). Values integrated over the full water column are compared. Open diamonds correspond to vertically integrated energy-flux convergences $\int (\partial\langle\tilde{v}\tilde{p}\rangle_\phi/\partial r) dz$ (i.e., an internal wave sink), solid diamonds to divergences (an internal wave source)—the solid diamond at 38 km was estimated assuming zero flux at the canyon head. Triangles denote vertically integrated microstructure turbulence production rates $\int \epsilon_p dz$, and dots Polzin et al. parameterized turbulence production rates (appendix) assuming mixing efficiency $\gamma = 0.2$. Vertical bars about the symbols correspond to one standard deviation about station means. Flux convergences are similar to those inferred by Petrucio et al. (1998) and microstructure turbulence production rates ϵ_p . They are 30 times larger than parameterized estimates. (bottom) Vertically integrated energy fluxes along the canyon axis.

steady state, weak advection, and neglecting local sources and leakage across the canyon sides

$$\nabla F_E \approx \frac{\Delta\langle\tilde{v}\tilde{p}\rangle_\phi}{\Delta r} = \epsilon_p = \epsilon - \langle w'b' \rangle = \epsilon(1 + \gamma), \quad (2)$$

where $F_E = \langle\tilde{v}\tilde{p}\rangle_\phi$ is the station-average upcanyon energy flux, \tilde{p} the internal-wave reduced pressure perturbation, Δr the along-axis station separation, ϵ_p the turbulence production rate, ϵ the turbulent kinetic energy dissipation rate, $\langle w'b' \rangle$ the turbulent diapycnal buoyancy flux, and $\gamma = 0.2$ the assumed mixing efficiency (Osborn 1980; Oakey 1982).

Depth-integrated, station-average versions of (2) are tested in the upper panel of Fig. 12. In the absence of fluxes across the canyon sides, which are not evident in Fig. 10, upcanyon energy fluxes decreasing up canyon (flux convergences, open diamonds) are an unambiguous signature of a turbulent sink (though, in the presence of sources, convergences provide at best a lower bound for the sink). Flux convergences are comparable to the microstructure estimates of turbulence production rates ϵ_p and a factor of roughly 30 larger than parameterized XCP–XCTD values. This reaffirms our previous assertion that the Gregg–Henyey–Polzin finescale scaling for turbulence does not apply in the canyon. Upcanyon energy fluxes increasing up canyon (flux divergences, solid diamonds) denote a net internal wave source (that could mask a weaker sink) comparable to the energy sinks in magnitude.

The canyon internal-wave energy budget in the canyon is not simply a matter of an upcanyon flux at the mouth decaying toward the head. Both sources and sinks must be present to explain the observed flux divergences and convergences. Possible energy sources include (i) internal tide generation by barotropic flow over canyon topography, (ii) focusing, and (iii) atmospheric forcing. There is no evidence for focusing of energy fluxes by the walls in the deep part of the canyon (Fig. 10). Winds were typically less than 10 m s^{-1} throughout the cruise (CG01) so seem an unlikely source. If internal tide generation is important, turbulence production rates may be controlled by this rate rather than an internal wave rate of transfer of energy toward small scales.

8. Summary

- Internal gravity waves in Monterey Canyon are an order of magnitude more energetic than typical open-ocean fields (Figs. 3 and 4). Available potential energy is especially elevated. Care must be taken to exclude the barotropic contribution to isopycnal displacements when calculating the baroclinic available potential energy. When this is done, the energy ratio KE–PE is close to the semidiurnal value of 2.13. The inferred barotropic displacements, found by least squares linear fitting the profiles with zero at the surface, are larger than expected for the reported 1 cm s^{-1} barotropic flows in the canyon.
- Near-inertial motions are absent; semidiurnal internal tides and their harmonics dominate (Fig. 2).
- Shear and strain levels do not covary (Figs. 5 and 8).
- Shear and strain are elevated by as much as an order of magnitude along the canyon axis in a stratified bottom boundary layer a few hundred meters thick (Figs. 6 and 7). Shear–strain ratios are consistent with a semidiurnal internal tide or a frequency spectrum of GM shape except near the bottom where strain estimates are contaminated by instrument noise because of the weak mean gradients below 900-m depth.
- Microstructure-inferred diffusivities are $100 \times 10^{-4} \text{ m}^2 \text{ s}^{-1}$ (Fig. 9), 30 times larger than those inferred from finescale parameterizations (Polzin et al. 1995; Sun and Kunze 1999). The parameterized results are robust to several approaches for estimating finescale shear and strain variances.
- The internal wave field is highly anisotropic. Phase-averaged horizontal energy fluxes $\langle\tilde{v}\tilde{p}\rangle_\phi$ are steered by canyon topography throughout the water column and are predominantly upcanyon (Figs. 10 and 11); fluxes are 5 kW m^{-1} at the mouth of the canyon (near the shelf break), weakening to about $\pm 1 \text{ kW m}^{-1}$ toward the shallow end. There is little indication of fluxes across the canyon sidewalls so that the internal tide energy balance in the canyon is approximately 1D. Fluxes increase upcanyon between some axis sta-

tions and, at one shallow station, are downcanyon, signifying local sources.

- Along-canyon energy-flux *convergences* ($\partial F_E/\partial r < 0$) are consistent with the microstructure turbulent dissipation rates ϵ (Fig. 12), suggesting a balance between flux convergence and a turbulent sink. However, comparable internal wave energy sources are indicated by along-canyon energy-flux *divergences* ($\partial F_E/\partial r > 0$). Likely candidates are local internal tide generation along the canyon axis and by rough topography. The sharp ridge and submarine fan proposed by Petrucio et al. (1998) do not appear to be sources.

9. Discussion

The crude energy budget attempted here (Fig. 12) raises a number of questions. We could not identify the source for the energy entering the mouth. Neither the sharp ridge nor the submarine fan proposed by Petrucio et al. (1998) appear to be viable candidates. Flux divergences imply both (i) generation farther down the continental slope that is focused up canyon, or (ii) local generation along the canyon. The decrease of upcanyon energy flux toward the canyon head is not monotonic, there even being downcanyon fluxes at the shallowest occupied station, indicating local energy sources within the canyon. These sources are unknown but doubtless involve interaction of surface tidal currents with rough topography. Both near-critical bottom slopes and large Baines (1982) forcing function $\nabla^2(1/h)$ are found at the canyon rim. However, there was no evidence for energy radiating from the rims; isopycnal displacements and turbulence are not elevated there, and the strong backscatter signal is thought to be due to euphausiids (Schoenherr 1991; CM). Near-critical bottom slopes are also found along the deeper canyon axis. Bottom scattering of the barotropic tide off the canyon's complicated topography is also likely but extant theories are based on either subcritical slopes (Bell 1975; Müller and Xu 1992; SG01) or two-dimensional topography (Prinsenber and Rattray 1975; Baines 1982; Craig 1987; Müller and Liu 2000) and so cannot be applied here.

It is unclear from our coarse spatial sampling whether upcanyon-propagating internal tides can negotiate sharp bends in the canyon axis. Fluxes appear to negotiate the deepest bend with little loss (Figs. 10 and 12) but are dramatically reduced at the next bend. Shallower stations are too close to bends to interpret. Webb and Pond (1986) showed that internal tides had no difficulty negotiating a right-angle bend in Knight Inlet with little back reflection. However, their channel was sufficiently narrow that they considered internal Kelvin waves (energy ratio 1) while, based on energy ratios of ~ 2 , we are dealing with free internal waves in Monterey Canyon. They suggested strong dissipation at the bends while CG found no enhancement of dissipation at the

sharp bends at the shallow end. It is possible that upcanyon energy flux is lost at the deepest bend then locally regenerated before the next cross-canyon section. An observational program designed to address how internal waves negotiate bends would be useful.

Turbulence in canyons is orders of magnitude stronger than that on the shelf away from banks (CG; Nash and Moum 2001), providing a potential pathway for nutrient fluxes into the euphotic zone. Given turbulent eddy diffusivities $K = 100 \times 10^{-4} \text{ m}^2 \text{ s}^{-1}$, water can communicate diffusively over 100 m in the vertical in only 10 days (as compared to a year or more in the open ocean). This timescale is comparable to the frequency of upwelling events.

The turbulent sink of internal wave energy was 30 times larger than predicted by open-ocean internal wave-wave interaction theory, indicating that the rate of energy transfer toward small scales is much larger in the canyon than in the open ocean. The canyon internal wave field differs from that of the open ocean. Rapid transfers to high wavenumber may also arise from reflection and scattering off the rough bathymetry; the barotropic tide can transfer energy directly to small scales by interacting with small-scale topography (Bell 1975). For 0.01 m s^{-1} barotropic flows (Petrucio et al. 1998), the response will be linear and semidiurnal for $k, U < \omega$ corresponding to topographic wavelengths $\lambda_r \gg 500 \text{ m}$, but become increasingly nonlinear at smaller topographic wavelengths.

A better understanding of the generation, propagation, and dissipation of internal waves is clearly important for quantifying turbulent mixing and nutrient fluxes in canyons. Interactions with the complicated topography of naturally occurring canyons need to be better understood. Given the apparent strong topographic steering of tidal currents (Rosenfeld et al. 1999; Key 1999), past estimates of up- and downcanyon mean flows based on Eulerian time means are suspect; from 63 measurements, Shephard et al. (1979) found 43 downcanyon and 26 upcanyon mean flows. Tracer-release experiments (e.g., Houghton and Ho 2001) are probably necessary to understand where water really goes in canyons.

Acknowledgments. The authors particularly thank Art Bartlett for his cool head in improving XCP deployment performance and repairs to XDP data acquisition hardware. The crew of the Point Sur performed admirably. Marla Stone, Mike Cook, and Scott Key assisted with the moored data deployment, processing and analysis. Cyndy Tynan, Jody Klymak, Patrick Cummins, and Charlie Eriksen are thanked for valuable suggestions and comments. Expendable (E. Kunze) and mooring (L. Rosenfeld) data from the canyon were collected and analyzed under NSF Grant OCE 96-33315. Expendable data on the continental slope were collected with support from ONR Grant N00014-97-I-0137. Microstructure

data were gathered and analyzed under NSF Grant OCE 96-33067 and ONR Grant N00014-97-1-0136.

APPENDIX

Finescale Parameterizations for Turbulence

Recent open-ocean studies have established a relationship connecting finescale vertical shear $\langle \tilde{V}_z^2 \rangle = \langle \tilde{u}_z^2 \rangle + \langle \tilde{v}_z^2 \rangle$ and strain $\langle \tilde{\xi}_z^2 \rangle$ variances with turbulent dissipation rates ϵ and eddy diffusivities K based on weak-triad (McComas and Müller 1981) and ray-tracing (Henyey et al. 1986) internal wave-wave interaction theory. These parameterizations imply that elevated turbulent mixing requires internal wave shear or strain variances above GM levels. In what follows, it is assumed that the eddy diffusivity $K = \gamma\epsilon/N^2$ (Osborn 1980) with mixing efficiency $\gamma = 0.2$ as is customary for high-Reynolds-number shear-driven turbulence (Oakey 1982).

a. Gregg (1989), shear only

Gregg (1989) was the first to verify the theoretical predictions of the form $\epsilon \sim E^2N^2$ using fine- and microstructure data. For the spectral level E , he used 10-m first-difference shear variances and found that

$$K = K_1 \frac{V_z^4}{GM V_z^4}, \tag{A1}$$

with empirical coefficient $K_1 = 0.052 \times 10^{-4} \text{ m}^2 \text{ s}^{-1}$ lying between McComas and Müller's and Henyey et al.'s predicted values. Gregg found that this scaling collapsed the data to within a factor of 2 for internal wave fields with GM frequency spectra. Gargett (1990) raised a number of issues about the appropriateness of using 10-m shear to estimate spectral level that have lead to using finescale spectral levels to quantify E .

b. Wijesekera et al. (1993), strain only

Wijesekera et al. found that Gregg's scaling underestimated the microstructure turbulent dissipation rate above the Yermak Plateau where tides and high-frequency wavepackets dominated the internal wave field. They suggested an ad hoc scaling in terms of strain variance,

$$K = K_2 \frac{\xi_z^4}{GM \xi_z^4}, \tag{A2}$$

where $K_2 = 0.052 \times 10^{-4} \text{ m}^2 \text{ s}^{-1}$. Parameterization (A2) has not proven successful elsewhere, possibly because of a greater role for permanent finestructure (vortical mode) in strain than shear (Polzin et al. 2001, submitted to *J. Phys. Oceanogr.*).

c. Polzin et al. (1995), shear and strain

Polzin et al. (1995) followed up a theoretical extension by Henyey (1991) that the rate of spectral transfer to high wavenumber depends on the "average" aspect ratio $\langle k_h/k_z \rangle$ of the wave field. The wave aspect ratio

$$k_h/k_z = [(\omega^2 - f^2)/(N^2 - \omega^2)]^{1/2}$$

is related to wave frequency ω , which in turn is related to the shear-strain ratio

$$R_\omega = \frac{V_z^2}{N^2 \xi_z^2} = \frac{(N^2 - \omega^2)(\omega^2 + f^2)}{N^2(\omega^2 - f^2)}$$

(Fofonoff 1969). The shear-strain ratio is thus a measure of the aspect ratio for single profile measurements. They derived a relationship depending on finescale shear and strain variance

$$K = K_3 \frac{V_z^4}{GM V_z^4} f(R_\omega), \tag{A3}$$

where $K_3 = 0.07 \times 10^{-4} \text{ m}^2 \text{ s}^{-1}$, $GM R_\omega = 3.0$, and

$$f(R_\omega) = \frac{R_\omega + 1}{GM R_\omega + 1} \sqrt{\frac{GM R_\omega^3 [1 - R_\omega + \sqrt{(R_\omega - 1)^2 + 8 R_\omega f^2 / N^2}]}{R_\omega^3 [1 - GM R_\omega + \sqrt{(GM R_\omega - 1)^2 + 8 GM R_\omega f^2 / N^2}]}}$$

This scaling collapsed oceanic variability to within a factor of two for wave fields with weakly non-GM frequency spectra.

d. Sun and Kunze (1999), shear and strain

Sun and Kunze reevaluated Henyey et al.'s (1986) ray-tracing simulations including test-wave interactions with background vertical divergence as well as vertical shear. They also obtained a parameterization in terms of finescale shear and strain variance,

$$K = K_4 \frac{V_z^4}{GM V_z^4} g(R_\omega), \tag{A4}$$

where $K_4 = (0.0012 - 0.003) \times 10^{-4} \text{ m}^2 \text{ s}^{-1}$,

$$g(R_\omega) = \left(\frac{R_\omega + 1}{R_\omega} \right)^2 \left[\text{arccosh} \left(\frac{N}{f} \right) + \frac{r_1 \arccos(f/N)}{\sqrt{R_\omega}} \right]$$

and $r_1 = 10-25$, depending on the degree of vertical and horizontal scale separation between the test waves (k_h, k_z) and the background wave field (K_H, K_z). The upper limit, found for vertical scale separation $k_z > K_z$,

reproduces the Polzin et al. (1995) results, which were observationally verified. The lower limit (for $k_z > 2K_z$ and $k_h > K_H$) produces turbulence production rates a factor of four smaller. Upper limits are used in the scatterplot (Fig. 8).

REFERENCES

- Allen, S. E., 1996: Topographically generated, subinertial flows within a finite-length canyon. *J. Phys. Oceanogr.*, **26**, 1608–1632.
- , C. Vindeirinho, R. E. Thomson, M. G. G. Foreman, and D. L. Mackas, 2001: Physical and biological processes over a submarine canyon during an upwelling event. *Can. J. Fish. Aquat. Sci.*, **58**, 671–684.
- Baines, P. G., 1973: The reflection of internal/inertial waves from bumpy surfaces. Part 2. Split reflection and diffraction. *J. Fluid Mech.*, **49**, 113–131.
- , 1982: On internal tide generation models. *Deep-Sea Res.*, **29**, 307–318.
- , 1983: Tidal motions in submarine canyons—A laboratory experiment. *J. Phys. Oceanogr.*, **13**, 310–328.
- Bell, T. H., 1975: Topographically-generated internal waves in the open ocean. *J. Geophys. Res.*, **80**, 320–327.
- Butman, B., 1986: An overview of the Lydonia Canyon experiment: Sediments, hydrography and currents. North Atlantic Slope and Canyon Study, Vol. 2, U.S. Geological Services Rep. MMS 86-0086, 156 pp.
- Cacchione, D., and C. Wunsch, 1974: Experimental study of internal waves over a slope. *J. Fluid Mech.*, **66**, 223–239.
- Cairns, J. L., and G. O. Williams, 1976: Internal wave observations from a midwater float. Part II. *J. Geophys. Res.*, **81**, 1943–1950.
- Carson, B., E. T. Baker, N. M. Hickey, C. A. Nittrouer, D. J. DeMaster, K. W. Thorbjarnarson, and G. W. Snyder, 1986: Modern sediment dispersal and accumulation in Quinault Submarine Canyon—A summary. *Mar. Geol.*, **71**, 1–13.
- Chen, X., and S. E. Allen, 1996: The influence of canyons on shelf currents: A theoretical study. *J. Geophys. Res.*, **101**, 18 043–18 059.
- Craig, P. D., 1987: Solutions for internal tidal generation over coastal topography. *J. Mar. Res.*, **45**, 83–105.
- Cummins, P. F., and L.-Y. Oey, 1997: Simulation of barotropic and baroclinic tides off northern British Columbia. *J. Phys. Oceanogr.*, **27**, 762–780.
- D'Asaro, E. A., and J. H. Morison, 1992: Internal waves and mixing in the Arctic Ocean. *Deep-Sea Res.*, **39** (Suppl. 2), 459–484.
- , and R.-C. Lien, 2000: The wave-turbulence transition for stratified flows. *J. Phys. Oceanogr.*, **30**, 1669–1678.
- Duda, T. F., and C. S. Cox, 1989: Vertical wavenumber spectra of velocity and shear at small internal wave scales. *J. Geophys. Res.*, **94**, 939–950.
- , and D. C. Jacobs, 1995: Comparison of shear measurements and mixing predictions with a direct observation of diapycnal mixing in the Atlantic thermocline. *J. Geophys. Res.*, **100**, 13 481–13 498.
- Eriksen, C. C., 1982: Observations of internal wave reflection off sloping bottoms. *J. Geophys. Res.*, **87**, 525–538.
- Fofonoff, N. P., 1969: Spectral characteristics of internal waves in the ocean. *Deep-Sea Res.*, **16** (Suppl.), 58–71.
- Freeland, H. L., and K. L. Denman, 1982: A topographically-induced upwelling center off southern Vancouver Island. *J. Mar. Res.*, **40**, 1069–1093.
- Garcia Lafuente, J., T. Sarhan, M. Vargas, J. M. Vargas, and F. Plaza, 1999: Tidal motions and tidally-induced fluxes through La Linea submarine canyon, western Alboran Sea. *J. Geophys. Res.*, **104**, 3109–3119.
- Gardner, W. D., 1989: Periodic resuspension in Baltimore Canyon by focussing of internal waves. *J. Geophys. Res.*, **94**, 18 185–18 194.
- Gargett, A. E., 1990: Do we really know how to scale the turbulent kinetic energy dissipation rate ϵ due to breaking of oceanic internal waves? *J. Geophys. Res.*, **95**, 15 971–15 974.
- , P. J. Hendricks, T. B. Sanford, T. R. Osborn, and A. J. Williams III, 1981: A composite spectrum of vertical shear in the upper ocean. *J. Phys. Oceanogr.*, **11**, 1258–1271.
- Garrett, C., and W. Munk, 1979: Internal waves in the ocean. *Annu. Rev. Fluid Mech.*, **11**, 339–369.
- Gordon, R. L., and N. F. Marshall, 1976: Submarine canyons: Internal wave traps? *Geophys. Res. Lett.*, **3**, 622–624.
- Gregg, M. C., 1989: Scaling turbulent dissipation in the thermocline. *J. Geophys. Res.*, **94**, 9686–9698.
- , and E. Kunze, 1991: Internal wave shear and strain in Santa Monica basin. *J. Geophys. Res.*, **96**, 16 709–16 719.
- , D. P. Winkel, and T. B. Sanford, 1993: Varieties of fully resolved spectra of vertical shear. *J. Phys. Oceanogr.*, **23**, 124–141.
- Heney, F. S., 1991: Scaling of internal wave model predictions for ϵ . *Dynamics of Oceanic Internal Gravity Waves: Proc. 'Aha Huliko'a Hawaiian Winter Workshop*, Honolulu, HI, University of Hawaii at Manoa, 233–236.
- , J. Wright, and S. M. Flatte, 1986: Energy and action flow through the internal wave field: An eikonal approach. *J. Geophys. Res.*, **91**, 8487–8495.
- Hickey, B. M., 1995: Coastal submarine canyons. *Topographic Effects in the Ocean: 'Aha Huliko'a Hawaiian Winter Workshop*, Honolulu, HI, University of Hawaii at Manoa, 95–110.
- Holloway, P. E., 1984: On the semidiurnal internal tide at a shelf-break region on the Australian north west shelf. *J. Phys. Oceanogr.*, **14**, 1778–1790.
- , 1996: A numerical model of internal tides with application to the Australian North West shelf. *J. Phys. Oceanogr.*, **26**, 21–37.
- Hotchkiss, F. S., and C. Wunsch, 1982: Internal waves in Hudson Canyon with possible geological implications. *Deep-Sea Res.*, **29**, 415–442.
- Houghton, R. W., and C. Ho, 2001: Diapycnal flow through the Georges Bank tidal front: A dye tracer study. *Geophys. Res. Lett.*, **28**, 33–36.
- Hunkins, K., 1988: Mean and tidal currents in Baltimore Canyon. *J. Geophys. Res.*, **93**, 6917–6929.
- Itsweire, E. C., T. R. Osborn, and T. P. Stanton, 1989: Horizontal distribution and characteristics of shear layers in the seasonal thermocline. *J. Phys. Oceanogr.*, **19**, 301–320.
- Kenney, R. D., and H. E. Winn, 1987: Cetacean biomass densities near submarine canyons compared to adjacent shelf/slope areas. *Cont. Shelf Res.*, **7**, 107–114.
- Key, S. A., 1999: Internal tidal bores in the Monterey Canyon. M.S. thesis, Naval Postgraduate School, Monterey, CA, 104 pp.
- Kinoshita, K., and M. Noble, 1995: The Monterey Submarine Canyon, California Moored Array Data Report. U.S. Geological Services Open File Rep. 95-838, 15 pp.
- Kinsella, E. D., A. E. Hay, and W. W. Jenner, 1987: Wind and topographic effects on the Labrador Current at Carson Canyon. *J. Geophys. Res.*, **92**, 853–869.
- Klinck, J. M., 1988: The influence of narrow transverse canyon on initially geostrophic flow. *J. Geophys. Res.*, **93**, 509–515.
- , 1989: Geostrophic adjustment over submarine canyons. *J. Geophys. Res.*, **94**, 6133–6144.
- , 1996: Circulation near submarine canyons: A modeling study. *J. Geophys. Res.*, **101**, 1211–1223.
- Kunze, E., and T. B. Sanford, 1996: Abyssal mixing: Where is it not? *J. Phys. Oceanogr.*, **26**, 2286–2296.
- , and J. M. Toole, 1997: Tidally driven vorticity, diurnal shear and turbulence atop Fieberling Seamount. *J. Phys. Oceanogr.*, **27**, 2663–2693.
- , M. A. Kennelly, and T. B. Sanford, 1992: The depth dependence of shear finestructure off Point Arena and near Pioneer Seamount. *J. Phys. Oceanogr.*, **22**, 29–41.
- Ledwell, J. R., A. J. Watson, and C. S. Law, 1993: Evidence of slow mixing across the pycnocline from an open-ocean tracer-release experiment. *Nature*, **364**, 701–703.
- Lien, R.-C., and M. C. Gregg, 2001: Observations of turbulence in

- a tidal beam and across a coastal ridge. *J. Geophys. Res.*, **106**, 4575–4591.
- Lueck, R. G., and T. R. Osborn, 1985: Turbulence measurements in a submarine canyon. *Cont. Shelf Res.*, **4**, 681–698.
- , and T. D. Mudge, 1997: Topographically-induced mixing around a shallow seamount. *Science*, **276**, 1831–1833.
- MacCready, P., and G. Pawlak, 2001: Stratified flow along a corrugated slope: Separation drag and wave drag. *J. Phys. Oceanogr.*, **31**, 2824–2839.
- MacKinnon, J. A., and M. C. Gregg, 2001: Mixing on the late-summer New England shelf: Solibores, shear and stratification. *J. Phys. Oceanogr.*, submitted.
- Maso, M., P. E. La Violante, and J. Tintore, 1990: Coastal flow modification by submarine canyons along the NE Spanish coast. *Sci. Mar.*, **54**, 343–348.
- McComas, C. H., and P. Müller, 1981: The dynamic balance of internal waves. *J. Phys. Oceanogr.*, **11**, 970–986.
- Müller, P., and N. Xu, 1992: Scattering of oceanic internal gravity waves off random bottom topography. *J. Phys. Oceanogr.*, **22**, 474–488.
- , and X. Liu, 2000: Scattering of internal waves at finite topography in two dimensions. Part I: Theory and case studies. *J. Phys. Oceanogr.*, **30**, 532–549.
- Munk, W., 1981: Internal waves and small-scale processes. *Evolution of Physical Oceanography*, B. A. Warren and C. Wunsch, Eds., The MIT Press, 264–291.
- Nabatov, V. N., and R. V. Ozmidov, 1988: Study of turbulence above seamounts in the Atlantic Ocean. *Oceanology*, **28**, 161–166.
- Nash, J. D., and J. N. Moum, 2001: Internal hydraulic flows on the continental shelf: High drag states over a small bank. *J. Geophys. Res.*, **106**, 4593–4611.
- Oakey, N. S., 1982: Determination of the rate of dissipation of turbulent energy from simultaneous temperature and velocity shear microstructure measurements. *J. Phys. Oceanogr.*, **12**, 256–271.
- Osborn, T. R., 1980: Estimates of the local rate of vertical diffusion from dissipation measurements. *J. Phys. Oceanogr.*, **10**, 83–89.
- Paduan, J. D., and L. K. Rosenfeld, 1996: Remotely-sensed surface currents in Monterey Bay from shored-based HF radar. *J. Geophys. Res.*, **101**, 20 669–20 686.
- Petruncio, E. T., L. K. Rosenfeld, and J. D. Paduan, 1998: Observations of the internal tide in Monterey Canyon. *J. Phys. Oceanogr.*, **28**, 1873–1903.
- Polzin, K., and E. Firing, 1997: Estimates of diapycnal mixing using LADCP and CTD data from I8S. *Int. WOCE Newsletter*, **29**, 39–42.
- , J. M. Toole, and R. W. Schmitt, 1995: Finescale parameterizations of turbulent dissipation. *J. Phys. Oceanogr.*, **25**, 306–328.
- , E. Kunze, J. M. Toole, and R. W. Schmitt, 2001: The partition of finescale energy into internal waves and geostrophic motions. *J. Phys. Oceanogr.*, submitted.
- Prinsenberg, S. J., and M. Rattray Jr., 1975: Effects of continental slope and variable Brunt–Väisälä frequency on the coastal generation of internal tides. *Deep-Sea Res.*, **22**, 251–263.
- Rhines, P., 1970: Edge-, bottom- and Rossby waves in a rotating stratified fluid. *Geophys. Fluid Dyn.*, **1**, 273–302.
- Rosenfeld, L., and E. Kunze, 1998: Internal waves in Monterey Canyon. *Extended Abstracts, Coastal Ocean Processes Symp.*, Woods Hole, MA, Woods Hole Oceanographic Institution, 10 pp.
- , F. Schwing, N. Garfield, and D. E. Tracy, 1994a: Bifurcated flow from an upwelling center: A cold water source for Monterey Bay. *Cont. Shelf Res.*, **14**, 931–964.
- , M. A. Noble, C. H. Pilskaln, and F. B. Schwing, 1994b: Currents in Monterey Submarine Canyon. *Eos, Trans. Amer. Geophys. Union*, **75**, 104.
- , R. E. Schramm, J. B. Paduan, G. A. Hatcher Jr., and T. Anderson, 1994c: Hydrographic data collected in Monterey Bay during 1 September 1988 to 16 December 1992. MBARI Tech. Rep. 94-15, 549 pp.
- , J. D. Paduan, E. T. Petruncio, and J. E. Goncalves, 1999: Numerical simulations and observations of the internal tide in a submarine canyon. *Dynamics of Oceanic Internal Gravity Waves II: Proc. 'Aha Huliko'a Hawaiian Winter Workshop*, Honolulu, HI, University of Hawaii, 63–72.
- Sanford, T. B., R. G. Drever, J. H. Dunlap, and E. A. D'Asaro, 1982: Design, operation and performance of an expendable temperature and velocity profiler (XTVP). Applied Physics Laboratory Tech. Rep. 8110, University of Washington, Seattle, WA, 83 pp. [Available from APL, University of Washington, 1013 NE 40th St., Seattle, WA 98105–6698.]
- , E. A. D'Asaro, E. Kunze, J. H. Dunlap, R. G. Drever, M. A. Kennelly, M. D. Prater, and M. S. Horgan, 1993: An XCP users guide and reference manual. Applied Physics Laboratory Tech. Rep. APL-UW TR 9309, University of Washington, Seattle, WA, 59 pp. [Available from APL, University of Washington, 1013 NE 40th St., Seattle, WA 98105–6698.]
- Schoenherr, J. R., 1991: Blue whales feeding on high concentrations of euphausiids around Monterey Submarine Canyon. *Can. J. Zool.*, **69**, 583–594.
- Shephard, F. P., N. F. Marshall, and P. A. McLoughlin, 1974: Currents in submarine canyons. *Deep-Sea Res.*, **21**, 691–706.
- , —, —, and G. G. Sullivan, 1979: *Currents in Submarine Canyons and Other Sea Valleys*. AAPG Studies in Geology, Vol. 8, American Association of Petroleum Geologists, 173 pp.
- Sherwin, T. J., 1988: Analysis of an internal tide observed on the Malin Shelf, north of Ireland. *J. Phys. Oceanogr.*, **18**, 1035–1050.
- , and N. K. Taylor, 1990: Numerical investigations of linear internal tide generation in the Rockall Trough. *Deep-Sea Res.*, **37**, 1595–1618.
- Smith, S. A., D. C. Fritts, and T. E. VanZandt, 1987: Evidence for a saturated spectrum of atmospheric gravity waves. *J. Atmos. Sci.*, **44**, 1404–1410.
- St. Laurent, L., and C. Garrett, 2002: The role of internal tides in mixing the deep ocean. *J. Phys. Oceanogr.*, in press.
- Sun, H., and E. Kunze, 1999: Internal wave–wave interactions: Part II. Spectral energy transfer and turbulence production rates. *J. Phys. Oceanogr.*, **29**, 2905–2919.
- Thorpe, S. A., 1996: The cross-slope transport of momentum by internal waves generated by alongslope currents over topography. *J. Phys. Oceanogr.*, **26**, 191–204.
- , 2001: Internal wave reflection and scatter from sloping rough topography. *J. Phys. Oceanogr.*, **31**, 537–553.
- Toole, J. M., K. L. Polzin, and R. W. Schmitt, 1994: Estimates of diapycnal mixing in the abyssal ocean. *Science*, **264**, 1120–1123.
- Torgrimson, G. M., and B. M. Hickey, 1979: Barotropic and baroclinic tides over the continental slope and shelf off Oregon. *J. Phys. Oceanogr.*, **9**, 945–961.
- Webb, A. J., and S. Pond, 1986: A modal decomposition of the internal tide in a deep, strongly-stratified inlet: Knight Inlet, British Columbia. *J. Geophys. Res.*, **91**, 9721–9738.
- Wijesekera, H., L. Padman, T. Dillon, M. Levine, C. Paulson, and R. Pinkel, 1993: The application of internal-wave dissipation models to a region of strong forcing. *J. Phys. Oceanogr.*, **23**, 269–286.
- Wunsch, C. H., 1968: On the propagation of internal waves up a slope. *Deep-Sea Res.*, **15**, 251–258.
- , 1969: Progressive internal waves on slopes. *J. Fluid Mech.*, **35**, 131–144.
- Xu, J. P., M. A. Noble, S. L. Eitrem, L. K. Rosenfeld, G. B. Schwing, and C. H. Pilskaln, 2002: Distribution and transport of suspected particulate matter in Monterey Canyon, California. *Mar. Geol.*, **181**, 215–234.